

Enhancing Reverse Intersystem Crossing with Extended Inverted Singlet-Triplet (X-*INVEST*) systems

Gaetano Ricci^a, Alessandro Landi^b, Juan Carlos Sancho-García^c, Yoann Olivier^a

^aLaboratory for Computational Modeling of Functional Materials, Namur Institute of Structured Matter, Université de Namur, Rue de Bruxelles, 61, B-5000 Namur, Belgium

^bDipartimento di Chimica e Biologia Adolfo Zambelli, Università degli Studi di Salerno, Via Giovanni Paolo II, I-84084 Fisciano (SA), Italy

^cDepartment of Physical Chemistry,
University of Alicante,
E-03080 Alicante, Spain

Abstract

The discovery of triangular-shaped organic molecules bearing an inverted singlet-triplet (INVEST) energy gap opened the way for a new strategy to increase the internal quantum efficiency of organic light-emitting diodes by enhancing the Reverse Intersystem Crossing (RISC) process thanks to a downhill process. However, all the molecular systems showing a negative ΔE_{ST} suffer from both a vanishing Spin-Orbit Coupling between the lowest singlet (S_1) and triplet (T_1) excited states and high energy differences with higher-lying singlet and triplet excited states, precluding their involvement in the spin conversion process.

In this work we proposed a new design strategy entailing the extension of the triangulene cores by connecting two INVEST triangulene units to form Uthrene- and Zethrene-like systems, doped with N and B atoms. A detailed inspection of the resulting molecular orbital distribution allowed rationalizing the electronic structure properties obtained employing wavefunction-based methods (NEVPT2, EOM-CCSD, SCS-CC2), showing how the Uthrene-like architecture can give origin to the energy proximity between the lowest singlet and triplet excited states, in some cases leading to their energy inversion. By feeding a kinetic model with the non-radiative rate constants calculated from *first principle* we showed how the Extended INVEST (X-INVEST) design strategy can open new pathways to boost the spin conversion process and the population of the emissive S_1 excited state.

1 Introduction

The pursuit of a strategy to fully harvest the singlet and triplet excitons upon electrical excitation is of primary importance to optimize the performance of Organic Light Emitting Diodes (OLEDs). The 1:3 ratio characterizing the number of microstates competing to the singlet and triplet spin-states translates in an imbalanced statistical population of the lowest singlet (S_1) and triplet (T_1) excited states. Following the Hund's rule,[1] in most of the organic molecular systems the singlet excited state bearing a given electronic configuration is located at higher energy than the triplet counterpart which forces 75% of the excitons to be trapped in the dark T_1 . It follows that the light emission can rely on the sole S_1 excitons, limiting the internal efficiency of light emission to 25%. Undoubtedly, this “spin-statistics limit” has represented one of the main challenges to overcome to promote the triplet to singlet conversion, known as Reverse Intersystem Crossing (RISC), and achieve 100% Internal Quantum Efficiency (IQE). It follows that in the molecular systems commonly employed in light-emitting devices, the S_1 - T_1 energy gap (ΔE_{ST}) is positive, forcing the RISC to be an up-conversion process. In this regard, several design strategies have been focused in reducing this energy gap to promote an easier conversion.[2]

Since the ΔE_{ST} is proportional to the spatial overlap between the hole and the electron wavefunctions, often matching the overlap between the Highest Occupied and Lowest Unoccupied Molecular Orbital (HOMO and LUMO, respectively), a legitimate strategy entails the design of organic systems where the hole and the electron are localized on different molecular fragments. Following this philosophy, donor-acceptor (D-A) compounds were designed by connecting through a single bond an electron-donating and an electron-accepting unit. Because of this molecular architecture, the hole (HOMO) and the electron (LUMO) are forced to be segregated on the donor and acceptor moieties, respectively. The resulting minimization of the ΔE_{ST} , caused by the reduction in the HOMO-LUMO overlap, allows for a thermally activated RISC and the harvesting of all the excitons into the bright S_1 state. This mechanism, known as Thermally Activated Delayed Fluorescence (TADF), [3] leads, in principle, to 100% IQE, resulting in a strategy able to increase the efficiency of OLEDs [4,5] without resorting to heavy metals. Nonetheless, the high flexible motion of the fragments about the bridging bond results in a broad fluorescence spectrum, representing a detrimental factor for color purity. Moreover, the poor HOMO-LUMO overlap, even though ensuring a small ΔE_{ST} , reduces the emission cross-section (or the oscillator strength, f_{osc}) of the emitting state, further limiting the applicability of D-A compounds in light-emitting devices. The contrasting dichotomy between ΔE_{ST} and f_{osc} was solved in 2016 by Hatakeyama *et al.* with the synthesis of a triangular shaped compound called DABNA-1 [6], where the electron donating and withdrawing effects of the nitrogen and boron atoms, respectively, resulted in a localization of the HOMO and LUMO on alternating atomic sites resulting in the S_1 and T_1 states exhibiting a Short-Range Charge Transfer (SRCT) character. Therefore, DABNA-1 exhibited a ΔE_{ST} as small as 0.15 eV and concomitantly a large f_{osc} . The latter effect was rationalized by Pershin *et al.* through a computational investigation, showing how the SRCT character allows the overlap of the tails of the hole and electron wavefunctions, large enough to guarantee a moderately large oscillator strength. [7] Moreover, this study firstly demonstrated that the employment of wavefunction-based methods accounting for double-excitations is the key to quantitatively predict the magnitude of the ΔE_{ST} in this Multi-Resonant (MR) TADF systems. Furthermore, an intriguing reduction in the ΔE_{ST} and an increase of the f_{osc} was forecasted by gradually extending the molecular core by merging two (or more) DABNA-1 cores. This promising design strategy was implemented by Hatakeyama *et al.* through the synthesis of ν -DABNA [8] (two connected DABNA-1 units) and later V-DABNA [9] (three connected DABNA-1 units),

reducing the ΔE_{ST} to 0.017 eV and 0.008 eV, respectively, along with a deep-blue ultra-narrow band emission, outstanding features for TADF emitters. The extension strategy has been recently pushed further in a computational study carried out by Pu and co. [10] where negative ΔE_{ST} values were predicted for linear extended DABNA-1 derivatives employing Time-Dependent Density Functional Theory (TD-DFT) with Double-Hybrid (DH) functionals.

Undoubtedly, the S_1 - T_1 energy inversion represents an appealing strategy to further enhance the performances of light-emitting devices, since in this condition the $T_1 \rightarrow S_1$ RISC process would be driven by an exothermic process. [11] Back in the 80s, experimental studies on two azaphenylene derivatives, doped with N atoms, namely cyclazine [12] and tri-aza-cyclazine, [13] suggested a potential realization of this inversion. Later, in 2019, a joint experimental and theoretical investigation on another N-doped triangle-shape compound, called heptazine, [14] provided no evidence of a triplet excited state below the lowest singlet excited state, suggesting that a violation of the Hund's rule can effectively take place in fully organic systems. These findings opened the doors to a new and challenging research line aimed at disclosing the fundamental causes of this inversion and realize it in molecular systems for OLED applications, as well as metal-free photocatalysis. [15-17]

The origin of the singlet-triplet inversion stems from the delicate interplay between the electron *exchange* interaction and electron *correlation* effects, which act on the ΔE_{ST} in an opposite direction. While the former stabilizes the triplet state with respect to the singlet one, thus adding a positive contribution to the energy gap, the latter arise from the opposite-spin electron interaction (*i.e.* Coulomb correlation), inducing a stabilization of the singlet state which, if large enough to overcome the exchange interaction, can promote the negative ΔE_{ST} . In his seminal work, de Silva [18] demonstrated that a minimal level of theory required to account for this electron correlation must introduce doubly-excited configurations, *i.e.* electronic configurations characterized by the simultaneous promotion of two electrons from the occupied to the virtual MOs. Consequently, quantum chemistry methods whose formalism is based on a single-excitation framework, such as Configuration Interaction of Singles (CIS) and the widely employed TD-DFT (either within the Tamm-Dancoff approximation, TDA-DFT or not), are unable to provide a correct description of these Inverted Singlet-Triplet systems, also known as INVEST. [19] Since then, several computational studies have been conducted on the three above-mentioned triangulenes, considered as prototypical INVEST compounds, and their derivatives, to benchmark the performances of different quantum chemistry methods. [20-23] The failure of TD(A)-DFT and CIS was systematically confirmed and the employment of wavefunction-based methods including doubly-excited configurations was tested, corroborating their ability to predict, either qualitatively or quantitatively, the negative ΔE_{ST} .

Unfortunately, because of their high point group symmetry, the triangulenes bearing a negative ΔE_{ST} were found to be unable to emit light, making them useless for OLED applications. In addition, the challenging synthesis of these triangular cores stimulated several theoretical groups to disclose rational design rules to enrich the chemical space of the INVEST family and find promising candidates exhibiting both singlet-triplet inversion and light emission ability. [24] In particular, the employment of High-Throughput Screening (HTS) assisted by Machine Learning algorithm allowed the identification of several INVEST emitters [25], not necessarily based on a triangular core [26-29]. It is worth mentioning that the HTS carried out by Aizawa *et al.*, [11] who identified and synthesized a heptazine derivative, HzTFEX2, showing an experimental $\Delta E_{ST} = -11$ meV and bearing a non-zero oscillator strength of the S_1 state.

Despite the valid contributions provided by these HTS-ML studies in discovering new INVEST emitters, the sole target properties were the ΔE_{ST} and the f_{osc} , neglecting the evaluation of the (R)ISC rate, which are equally crucial for assessing the applicability of these compounds in OLEDs. As already observed in D-A and MR-TADF molecules, the similar nature of the S_1 and T_1 characterizing the INVEST cores leads to a spin orbit coupling (SOC) between these

two states to vanish, in the limit of the Condon approximation where no vibronic coupling is involved, hampering direct spin conversion. Therefore, the involvement of intermediate higher-lying singlet or triplet excited states either via direct population or through vibronic coupling is often invoked to promote singlet-triplet conversion and to ensure the population of S_1 , [30] questioning the actual utility of the negative ΔE_{ST} (Figure 1). The introduction of substituents to the core might aid the enhancement of the spin conversion process through a modulation of the nature of the S_1 and T_1 excited states, enhancing SOC and potentially activating the direct pathway or by introducing substituent states which could act as intermediate excited states during the interconversion process. For instance, the experimental RISC rate measured for the substituted heptazine, HzTFEX2, reached a remarkable value of $2.3 \cdot 10^7 \text{ s}^{-1}$. [11] Nonetheless, the selection of the substituents is not trivial and should be rationally conducted to avoid the enhancement of a property at the expenses of another, *e.g.* the magnitude and sign of the ΔE_{ST} as well as the oscillator strength.

In this regard, it is worth mentioning that whatever the way higher-lying excited states are involved in the singlet-triplet conversion, the energy spacing within the singlet and the triplet manifolds of excited states is crucial.[32, 50] Considering the direct mechanism and the quantum nature of the conversion process within the Fermi Golden rule framework, it was evidenced in heptazine and derivatives that a fast RISC does not necessarily require a largely negative ΔE_{ST} but rather energy resonance between the vibrational levels of the electronic states involved as well as maximized overlap between the vibrational wavefunctions. [31,32] Besides intermediate higher-lying triplet states, displaying a large negative S_1 - T_n energy gap, on one hand would not ensure this energy resonance and likely results in a small S_1 - T_n rate falling in the Marcus inverse regime, and on the other hand would entail a small endothermic $T_1 \rightarrow T_n$ reverse IC rate, overall leading to limited spin conversion considering such an indirect path. In our previous study, we obtained small $T_2 \rightarrow S_1$ RISC rate ranging from 10^3 to 10^4 s^{-1} for three cyclazine derivatives, bearing an S_1 - T_2 energy gap $\approx -0.8 \text{ eV}$ suggesting that for such large energy gap, RISC takes place in the Marcus inverse regime. Going beyond the Condon approximation would allow the contribution of higher-lying triplets through vibronic coupling without requiring their direct population. Marian and coworkers showed that a substantial increase of the $T_1 \rightarrow S_1$ RISC rate can be observed by accounting for Herzberg-Teller effects for heptazine and one of his derivatives, HAP-3MF. [32] Interestingly, disclosing structure-property relationship leading to INVEST systems with an intrinsic high RISC rate remains quite challenging. However, a reasonable strategy would encompass the design of compounds with closely-lying singlet and triplet excited states to speed up spin conversion since all the mechanisms invoked strongly depends on the energy differences between states.

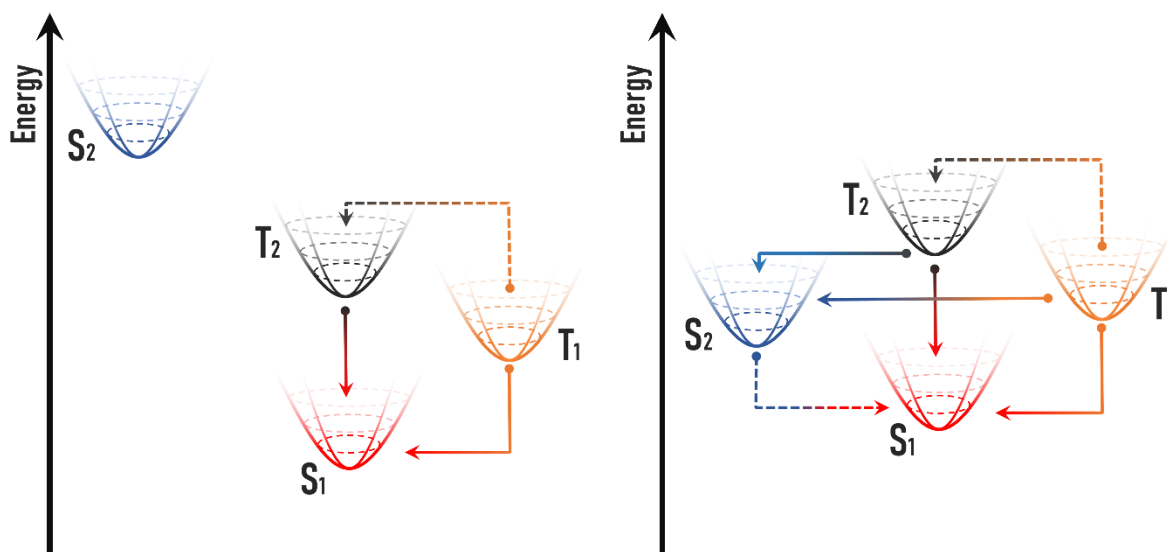


Figure 1: (left) the energy diagram of a single-core INVEST compound; (right) the energy diagram of an extended INVEST compound. The solid lines represent RISC pathway, and the dashed lines represent IC pathway.

In our previous study, [24] we showed that merging two triangular INVEST cores to build a Uthrene-like molecule can be a valid strategy to break the symmetry constraints and obtain a non-zero f_{osc} along with a non-vanishing S_1 - T_1 SOC. Moreover, the extension process brings the S_1 , S_2 , T_1 and T_2 excited states in an energy proximity such as the S_2 state potentially lies below T_1 . Among the possible ISC pathways, the $T_1 \rightarrow S_2$ turned out to have the highest rate thanks to the high SOC and small (and negative) energy gap between these two states. It follows that, as observed with MR-TADF compounds, the extension of the molecular core is a fruitful strategy to improve the photophysical properties of the molecular systems. In this particular case, new channels become available for the population of S_1 (Figure 1), with the RISC process occurring via a new and alternative pathway involving a fast $T_1 \rightarrow S_2$ ISC followed by an ultra-fast $S_2 \rightarrow S_1$ Internal Conversion (IC). This suggests that extended INVEST cores here named X-INVEST is a design strategy that can open new doors for a fast spin conversion, defining a new paradigm for the RISC process. Note that we already evaluated the effect of the extension of the triangulene core by systematically enlarging the perimeter of an INVEST molecule, [20] showing how this strategy can effectively promote a more negative ΔE_{ST} . The same was done by Domke *et al.* [33] by gradually increasing the perimeter of hexagonal molecule doped with B and N, promoting the S_1 - T_1 inversion. However, these two strategies keep retaining the same high D_{3h} symmetry of the core, with no effect on the oscillator strength and energy spacing among the lowest singlet and triplet excited states. It follows that the extension procedure should induce a lower symmetry to achieve the goals sought.

In this work, we aim at investigating from a computational point of view the electronic structure and the photophysical properties of a series of organic compounds obtained by merging two triangulene units known to bear a negative ΔE_{ST} . Specifically, we will adopt a parallel and an antiparallel orientation when connecting the two triangulenes to form Uthrene-like and Zethrene-like structures (Figure 2), doped with N and B atoms. The pristine systems, Uthrene and Zethrene, are isomeric carbon-based materials. While the latter is a Kekulé molecule with a closed-shell ground-state, the former is non-Kekulé compound showing a biradical character in the ground-state, a feature revealed to be related to the degree of electron correlation. In particular, Uthrene has recently gained attention being the smallest graphene nanoribbons having a non-planar structure. [34]

The manuscript is organized as follows: in section 3 we will benchmark the performances of three wavefunction-based methods on two reference extended compounds to identify the most suitable computational protocol to study the electronic structure of these systems. In section 4, we will carry out a detailed analysis of the MOs distribution resulting from the extension process and rationalize the energy gap between singlets and triplets. In section 5 we will assess and rationalize the singlet-triplet energy gaps obtained with the quantum chemical calculations. Finally, in section 6, we will model the spin conversion dynamics of the most promising X-INVEST compounds by computing the (R)ISC rates from first principles and building a kinetic model to analyze the pathways mainly contributing to the S_1 population. Considering the prominent contribution of the S_1 - S_2 IC in the spin conversion process (*vide infra*), quantum dynamics simulations have been carried out to validate the rate constants calculated within the Fermi's Golden Rule.

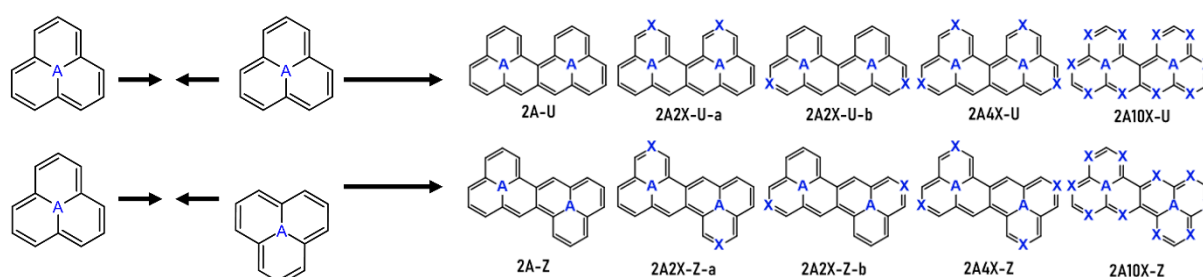


Figure 2: Connection orientation and molecular structures of the compounds investigated in this work. The top structures are related to the Uthrene-like systems (-U) and the bottom structures to the Zethrene-like systems (-Z). A = N or B and X = N or B.

2 Methods

All the structures at the ground state and excited state have been optimized using DFT and TDA-DFT, respectively, employing PBE0 functional and def2-SVP basis set. All real frequencies have been obtained. The vertical excitation energies at the ground state geometries have been computed employing Spin Component Scaling [35] 2nd order Coupled Cluster (SCS-CC2), [36] Equation Of Motion Coupled Cluster (EOM-CCSD), [37] State Averaged Complete Active Space Self Consistent Field (SA-CASSCF) [38] and Strongly Contracted 2nd order N-Electron Valence Perturbation Theory (SC-NEVPT2). [39] For the latter two methods, active space of (8,8), (10,10) and (12,12) have been tested. The total excited state energies at the excited state optimized geometries have been computed at NEVPT2(12,12) level. All the excited state calculations have been carried out employing def2-TZVP basis set. The RI-JK approximation employing the def2/JK auxiliary basis set has been used for the CASSCF and NEVPT2 calculations as implemented in ORCA 5.3.0. [43] The SOC matrix elements have been computed at CASSCF(12,12) level at the ground state geometry. Both CASSCF and NEVPT2 calculations were carried out requesting five roots for both singlet and triplet multiplicities. The SCS-CC2 calculations were conducted with Turbomole 7.4. [40] The EOM-CCSD, the Herzberg-Teller corrections and the non-adiabatic couplings were computed with Q-Chem 5.4. [41] For the former method, the frozen core approximation and the Frozen Natural Orbital approximation [42] (FNO, with 98% of natural virtual orbital space introduced) have been employed to speed-up the calculation. The exchange interaction integrals were computed employing Multiwfn 3.8. [45] The non-radiative decay constants associated with the elementary conversions (both between same-multiplicity and different-multiplicity excited

states, namely IC and (R)ISC) were calculated within the Thermal Vibration Correlation Function (TVCF) formalism including the Duschinsky rotation at 298 K using FCClasses 3.0.3. [44] The calculation of the IC rate through the TVCF formalism was validated through quantum dynamics simulations on two cases. Quantum dynamics calculations have been performed by solving the time-dependent Schrödinger equation ($-i\hbar(dC/dt) = HC$) with an orthogonalized Krylov subspace method, [51] including almost the whole set of vibrational coordinates though a careful partitioning of the whole vibronic space in subspaces of increasing dimensionality [52-54], see also Supporting Information for more details.

3 Definition of the computational protocol

The correct description of the double excitations in treating the electronic structure of the INVEST systems is of crucial importance. Recently, Jacquemin *et al.* [21] benchmarked a series of single-reference coupled cluster methods on cyclazine, pentazine, heptazine and boron and nitrogen-doped derivatives of these molecules showing the tendency of the SCS-CC2 to overestimate the negative ΔE_{ST} with respect to the more sophisticated EOM-CC3. These results are in line with our previous works, where we showed that SCS-CC2 overestimates the negative ΔE_{ST} of N-doped triangulenes and especially pentazine with respect to SC-NEVPT2 and ADC(3). [24] Interestingly, Jacquemin *et al.* further confirms that SC-NEVPT2/def2-TZVP and EOM-CCSD/aug-cc-pVTZ tend to provide ΔE_{ST} in satisfying agreement with EOM-CC3, suggesting that they could serve as reference methods, especially for larger size systems. However, a careful selection and convergence of the active space is strongly recommended for methods based on a multi-configurational and multi-reference formalism, such as CASSCF and NEVPT2, for which the ΔE_{ST} magnitude exhibits a high sensitivity to the number of active orbitals and electrons. Studying a series of single core triangulenes, Pernal *et al.* [46] showed that by increasing the active space (from 2,2 to 6,6 and finally 14,14) the ΔE_{ST} computed at CASSCF reduces, moving from positive to negative values. At the same time the NEVPT2 energy gap tends to gradually decrease in line with previous results obtained by us [24] in pentazine and others in cyclazine and heptazine. [22,46]

It follows that the reliability of the predicted singlet-triplet energy gap magnitude is still a debate and an accurate selection of the level of theory, accounting for both accuracy and computational cost, is crucial to avoid misdescription of the electronic structure of INVEST compounds. A further complication arises in the context of the present study considering that the reliability of the level of theory must address not only the S_1 - T_1 gap, but also the one involving S_2 and T_2 to properly describe the kinetics of the different electronic processes governing the population of these excited states and finally the dynamics of the whole triplet harvesting mechanism. In this regard, we compared the performance of EOM-CCSD and NEVPT2(12,12) in predicting the energy gap between the excited states for two reference extended derivatives, namely 2N-U and 2N-Z, obtained by merging two cyclazine core according to the scheme in Figure 2. The choice of the active space has been made after a careful check on the convergence of the singlet-triplet energy gaps (see Table S5). In addition, (SCS-)CC2 and the dependency of NEVPT2 on the active space size have been evaluated and are presented in the Supporting Information (Tables S4, S5 and S6).

Table 1 shows the EOM-CCSD and NEVPT2(12,12) vertical excitation energies of S_1 , S_2 , T_1 and T_2 and the resulting energy gaps computed at the ground state geometry for the 2N-U and 2N-Z compounds.

Table 1: S_1 , S_2 , T_1 , T_2 vertical excitation energies at the S_0 geometry, S_1 - S_2 , T_1 - T_2 , S_1 - T_1 and S_2 - T_2 energy gaps computed at EOM-CCSD and NEVPT2(12,12) levels of theory using def2-TZVP basis set for the 2N-U and 2N-Z.

	S_1 (eV)	S_2 (eV)	T_1 (eV)	T_2 (eV)	$\Delta E(S_1-S_2)$ (eV)	$\Delta E(T_1-T_2)$ (eV)	$\Delta E(S_1-T_1)$ (eV)	$\Delta E(S_2-T_2)$ (eV)
<i>EOM-CCSD</i>								
2N-U	1.754	1.765	1.668	1.771	-0.011	-0.103	0.086	-0.006
2N-Z	1.305	2.942	0.958	1.940	-1.637	-0.982	0.347	1.002
<i>NEVPT2(12,12)</i>								
2N-U	1.544	1.576	1.539	1.585	-0.032	-0.043	0.005	-0.009
2N-Z	0.780	1.520	0.707	1.517	-0.740	-0.810	0.073	0.003

We start the comparison focusing on the 2N-U molecule. EOM-CCSD systematically predicts larger excitation energies with respect to NEVPT2(12,12). However, the energy gaps between excited states are predicted to be slightly different by the two levels of theory, with the largest discrepancies exhibited by the energy gaps involving the T_1 state (see Table 1). Interestingly, at NEVPT2(12,12) level, S_1 and T_1 are not described by the same electronic configuration, since the former is dominated by a HOMO \rightarrow LUMO transition while the latter by a HOMO \rightarrow LUMO+1 transition. The triplet counterpart of S_1 is T_2 (see Table S2), so that the energy gap between these two states is effectively negative (-0.044 eV) at NEVPT2 level. On the contrary, T_1 and S_2 share the same HOMO \rightarrow LUMO+1 transition, but while for the former the contribution is $> 70\%$, the latter receives contribution as well from the HOMO-1 \rightarrow LUMO transition. The different nature characterizing the two excited states leads to an increase of the exchange interaction, in turn inducing the positive S_2 - T_1 gap (0.097 eV).

Moving now to 2N-Z, from Table 1 we observed that EOM-CCSD overestimates the S_1 , S_2 , T_1 and T_2 excitation energies compared to NEVPT2(12,12). The tendency to overshoot the singlet excitation energies is common for EOM-CCSD. [47] However the large difference (larger than 1 eV) related to S_2 is characteristic of the large amount (as large as 50%) of double excitations contributing to the CASSCF excited states wavefunctions (see Figure S3) which thus requires a multiconfigurational treatment. Therefore, the energy gaps computed at the EOM-CCSD level of theory involving especially S_2 are largely overestimated as compared to NEVPT2(12,12). Such an energy discrepancy associated with the S_2 state of 2N-Z hinders the use of EOM-CCSD throughout this work and suggests using NEVPT2(12,12) as the method of reference to ensure a balanced description of the Uthrene- and Zethrene-like compounds thanks to reliable treatment of the static and the dynamical electron correlation effects and its good trade-off between computational cost and accuracy.

4 Rationalization of the excited energy gaps in N-centered and B-centered extended systems

In this section, we aim at rationalizing the much denser manifolds of singlet and triplet excited states in Uthrene-like as compared to Zethrene-like compounds based on a detailed analysis of the molecular orbitals (MOs) localization. Specifically, we focus on the HOMO-1, HOMO, LUMO and LUMO+1 MOs of the extended compounds since they are involved in the one-electron transitions describing the above-mentioned excited states (see Table S2). We consider 2N-U and 2N-Z as reference compounds and build their MOs as the “+” and “-” combinations of the HOMO and LUMO orbitals of cyclazine (Figure 3). For simplicity and without loss of generality, the orbitals distributions of the starting building blocks are obtained from a Hückel

calculation. The order and the energy spacing between the resulting extended MOs can be deduced by evaluating the change in the bonding, anti-bonding and non-bonding character going from the single core to the extended compounds. More specifically, the overlap between the single-core MOs enclosed in the connection area (represented by the darker colors in Figure 3) determines the magnitude of the HOMO (LUMO) electronic interaction, in turn dictating the orbital energy change going from the single core to the extended compounds. Nonetheless, the extension unavoidably induces a reorganization of the electron density on the peripheral atomic sites, therefore the resulting MOs do not fully resemble those of the original building blocks.

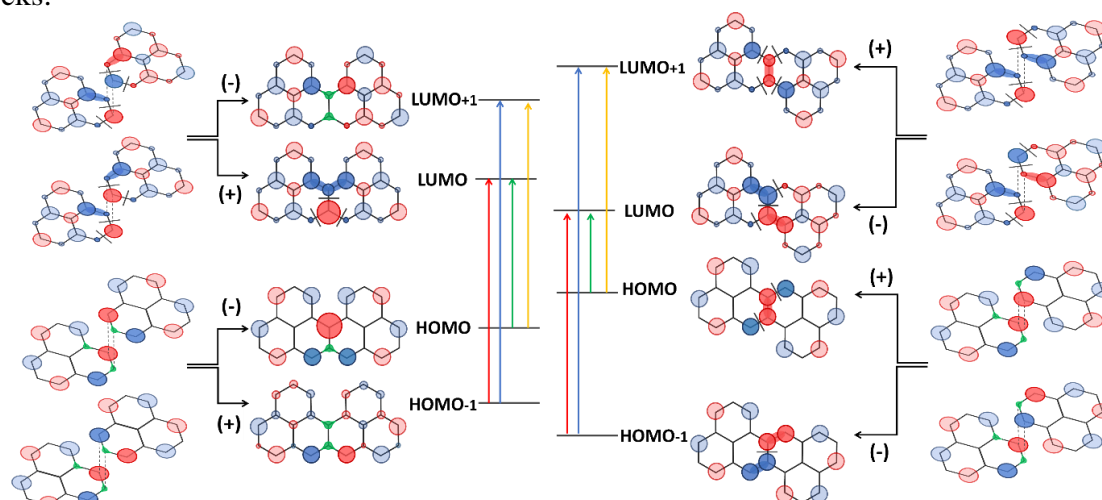


Figure 3: MOs diagram of the 2N-U (left) and 2N-Z (right) system built by combining the molecular orbitals of the single-core triangulene. The MOs of the single-core and the extended system are obtained by a Hückel calculation. The atomic centers involved in non-bonding interactions are highlighted in green. The bonds involved in a bonding interaction are highlighted by a colored stick along the bond, while those involved in an anti-bonding interaction are crossed by a black stick.

Interestingly, 2N-U and 2N-Z compounds present noticeable differences in their MOs distribution. As it can be observed in Figure 3, the connection occurring with a parallel orientation, giving rise to a Uthrene-like structure, leads the (+) combination of the HOMOs of the cyclazine units to superimpose atomic sites bearing Linear Combination of Atomic Orbital (LCAO) coefficients with the same magnitude but opposite signs. This leads the HOMO-1 in 2N-U to display a nodal plane passing through the connection area. The same occurs with the (-) combination of the LUMO of the cyclazine units. Interestingly, the (-) combination of the HOMOs of the cyclazine units retains the non-bonding character in 2N-U, contrarily to the (+) combination of the LUMOs, for which the resulting extended orbital does not present any nodal sites, making this MO the sole lacking the non-bonding interaction in the Uthrene-like system. A completely different picture emerges from the anti-parallel orientation, giving rise to a Zethrene-like structure, where none of the combinations of either HOMOs or LUMOs of the cyclazine units forces the reciprocal cancellation of LCAO coefficients of the superimposed atomic sites. It follows that the resulting extended MOs present only bonding and anti-bonding interactions in the connection region.

This difference in electron density distribution in the connection region has a significant impact on the energy difference between the MOs, in turn affecting the excited state energies. In 2N-U, the weak modulation of the non-bonding character going from HOMO-1 to HOMO and the modulation from the non-bonding to anti-bonding character from the LUMO to the LUMO+1 results in a small energy difference between these orbitals (see the left diagram in Figure 3 and Table S1). In 2N-Z, a different scenario occurs. Going from HOMO to HOMO-1 (LUMO to

LUMO+1), we observe an increase of the anti-bonding interactions and a decrease of the bonding interactions in the connection region, which causes a larger energy difference between these two occupied (unoccupied) MOs (see the right diagram in Figure 3 and Table S1). Therefore, the energy gaps between the S_1 , T_1 , S_2 and T_2 excited states are readily rationalized based on the energy differences between the HOMO-1 and the HOMO and the LUMO and the LUMO+1 orbitals. Specifically, the small (large) energy gap between HOMO–HOMO-1 and LUMO-LUMO+1 reflects the small (large) S_1 - S_2 and T_1 - T_2 energy gaps in 2N-U (2N-Z). Interestingly, thanks to the strong non-bonding nature of the HOMO in the 2N-U, this orbital is only weakly destabilized with respect to the HOMO orbital of cyclazine. The absence of the non-bonding character in the HOMO of 2N-Z results in a large destabilization of this orbital with respect to the HOMO of cyclazine. It follows that the HOMO-LUMO gap in the 2N-U is larger than the one in the 2N-Z (Figure 3), reflecting the higher excitation energies predicted for the former than the latter at NEVPT2 (Tables 1 and 2). When comparing the S_1 excitation energies of 2N-U, 2N-Z and cyclazine, as obtained at NEVPT2 level, we observed that while cyclazine has a larger S_1 energy (1.090 eV) than 2N-Z (0.780 eV) in line with the trend in band gaps (5.82 eV and 7.06 eV for 2N-Z and cyclazine respectively), the excitation energy of 2N-U is larger than the one of cyclazine despite its smaller band gap (6.95 eV). It is worth highlighting that this trend is not related to electron correlation effect since it is retained as well at CIS level (see Table S6). This apparent discrepancy can be rationalized resorting to a two-state model (equation S1.1), observing that the larger excitation energy in 2N-U is related to the smaller magnitude of the Coulomb integrals (J_{HH} , J_{HL}) with respect to cyclazine as a result of the spread and thus a dilution effect of the frontier orbitals in 2N-U. The exchange integral values (K_{HL}) and the HOMO-LUMO gap are comparable for the two compounds (see Table S7). This trend is also observed for the T_1 excitation energies for 2N-U, 2N-Z and cyclazine (1.539 eV, 0.707 eV and 1.193 eV, respectively, at NEVPT2 level) for the same reason. We rationalized the magnitude of the S_1 - T_1 and S_2 - T_2 gaps by computing the exchange interaction energy (see Table S8) between the pair of occupied and unoccupied MOs. The magnitude of the exchange interaction is elucidated by the weaker MOs overlap in 2N-U with respect to 2N-Z, due to the presence the more pronounced non-bonding character, especially in the connection region, in the MOs of the former as compared to the latter. The replacement of the two N with two B atoms in the Uthrene- and Zethrene-like systems lead to the compounds 2B-U and 2B-Z, respectively, both having four less electrons than 2N-U and 2N-Z. It is worth noticing that, at single-core level, the replacement of the N atom with a B one on the central atom leads to a system with two electrons-less than cyclazine. In both single-core triangulenes, the frontier MOs can be built by combining the orbitals of the parent [12]annulene and the single p_z atomic orbital of the N or the B atom. As shown in Figure S4, the a_2'' orbital of [12]annulene can be combined with the p_z orbital of the heteroatom, while the a_1'' orbital of the parent compound remains unaltered, keeping the *non-bonding* character. It follows that the two MOs in the triangulene compound resulting from the combination with the p_z (either N- or B-centered) differ only in the phase of the linear combination but bear the same electron density distribution. In light of this, in cyclazine and in the B-centered counterpart, the non-bonding character is displayed by the HOMO and the LUMO, respectively, while the orbital mainly localized on the atomic sites showing a node in the non-bonding orbital is the LUMO and the HOMO, respectively. It follows that in both the single-core triangulenes, the complementary distribution of the electron density is retained within the two frontier MOs. In this regard, the electron density distribution characterizing the occupied (unoccupied) MOs in 2N-U and 2N-Z will describe the orbital pattern in the unoccupied (occupied) MOs in 2B-U and 2B-Z. We can construct the same diagram of Figure 3 for the B-centered extended systems, considering them as arising from the connection of two B-centered cyclazine units (*i.e.* a

cyclazine with the N atom replaced by a B atom). The resulting MOs diagram is shown in Figure 4.

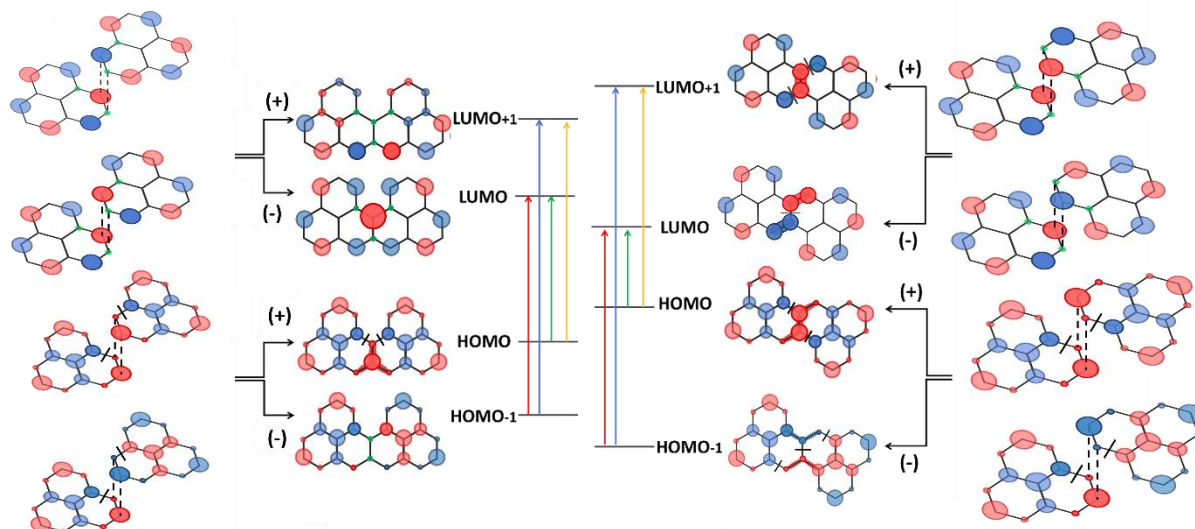


Figure 4: MOs diagram of the 2B-U (left) and 2B-Z (right) system built by combining the molecular orbitals of the single-core B-centered triangulene. The MOs of the single-core and the extended system are obtained by a Hückel calculation. The atomic centers involved in non-bonding interactions are highlighted in green. The bonds involved in a bonding interaction are highlighted by a colored stick along the bond, while those involved in an anti-bonding interaction are crossed by a black stick.

As can be observed, for both 2B-U and 2B-Z the orbitals distributions are complementary to the one of 2N-U and 2N-Z (Figure 3), *i.e.* the HOMOs (LUMOs) of the former ones are localized on the atomic sites where the latter ones have a high LUMOs (HOMOs) density. Specifically, in 2B-U the non-bonding orbitals are now the LUMO and LUMO+1, while the HOMO-1 presents a nodal plane passing through the connection area (as occurred in the LUMO+1 of 2N-U) and the HOMO exhibits only bonding and anti-bonding distribution (as the LUMO in 2N-U). For the 2B-Z, as we observed for 2N-Z, the non-bonding character is absent in all the MOs, which show the bonding and anti-bonding redistribution moving from the HOMO-1 to the HOMO and from the LUMO to the LUMO+1. Consequently, the relative energy between MOs follows the same scheme observed for the N-centered extended system, leading the 2B-U and 2B-Z to share the same electronic structure features as 2N-U and 2N-Z, respectively.

The analysis carried out in this section clearly shows how the electronic structure of the extended systems is strongly dependent on the symmetry of the connection, which in turn will define a different picture of the spin conversion. Specifically, the presence of the non-bonding character found in the Uthrene-like MOs ensures the energy proximity of the singlet and triplet excited states useful for enhancing the overall RISC rate for the population of the S_1 state.

5 N-doped N-centered and B-centered extended systems: impact on the excited state energy landscape

In this section we will investigate the electronic structure of N-centered and B-centered extended compounds doped with N and B (see Figure 2). All the compounds reported here

actually result from the connection of two identical single core triangulene units known to bear a negative S_1 - T_1 energy gap (see Figure 2 and Figure S5).

From Figure S1 it can be seen that the distribution of the electron density of the four MOs obtained at the Hartree-Fock level using the def2/TZVP basis for the 2N-U and the 2N-Z resembles the Hückel orbitals (see Figure 3), with the 2N-U orbitals displaying a non-bonding pattern in the HOMO, HOMO-1 and LUMO+1 orbitals within the central part of the molecule, while this feature is missing in the Zethrene-like compounds. This suggests that the MOs scheme shown in Figure 3 is expected to be retained for the other extended compounds, considering that the single-core N-doped compounds retain the orbital distribution of the parent cyclazine and B-centered counterpart (see Figure S5).

For both families of molecules, NEVPT2(12,12)/def2-TZVP calculations (see Table 3) predict that the introduction of two (resulting in compounds 2N2N-U_a and 2N2N-U_b for the Uthrene-like family and 2N2N-Z_a and 2N2N-Z_b for the Zethrene-like family) to four nitrogen (2N4N-U and 2N4N-Z compounds) atoms on the vertices of the triangulene units containing a nitrogen in its center results in a systematic decrease of the singlets and triplets excitation energy. This originates from the asymmetric stabilization of the LUMO and LUMO+1 (Table S1 and Figure S2) as compared to the HOMO and HOMO-1. While the HOMO and HOMO-1 are weakly stabilized due to inductive electron withdrawing effects, the LUMO and LUMO+1 are stabilized to a larger extent due to the pronounced mesomeric electron withdrawing effects caused by N atoms sitting on atomic centers bearing a high weight in the MOs of 2N-U. Contrarily, 12N-U and 12N-Z show a strong blue-shift with respect to 2N-U and 2N-Z because of the stronger stabilization of the HOMO₋₁ and HOMO orbitals due again to the dominant mesomeric electron withdrawing effects caused by the substitution of nitrogen atoms on the atomic sites bearing a high density of these MOs, while the LUMO and LUMO+1 exhibit a weaker stabilization (Table S1 and Figure S2). It is interesting again to observe the inductive effect coming from the introduction of the N atoms, which produces an overall stabilization of all the frontier MOs (see Figure S2).

In contrast, with N-centered extended systems, mesomeric effects due to nitrogen doping on the vertices of the extended triangulenes cores of B-centered extended systems are acting on the HOMO and the HOMO-1, while leaving the LUMO and the LUMO+1 almost unaffected (see Table S1). This is due to the electronic structure of the 2B-U and 2B-Z where the non-bonding orbital of the single core and the orbital showing a complementary pattern are inverted as compared to 2N-U and 2N-Z (see Figures 3 and 4). It follows that the nature and position of the heteroatoms can easily modulate the energy of the excited states, allowing for multiple possibilities for the color-tuning. Note that the introduction of boron atoms on the periphery, either in N- or B-centered compounds, results in a distorted molecular structure losing the high symmetry of the single core and thus likely resulting in a large positive ΔE_{ST} . For this reason, these compounds are not considered in the study.

Table 3: S_1 , S_2 , T_1 , T_2 vertical excitation energies, S_1 - T_1 , S_2 - T_2 energy gap and oscillator strength values (in parentheses) computed at NEVPT2(12,12)/def2-TZVP level of theory at the ground state geometry of the Uthrene-like and Zethrene-like compounds.

	S_1 (eV)	S_2 (eV)	T_1 (eV)	T_2 (eV)	$\Delta E(S_1-T_1)$ (eV)	$\Delta E(S_2-T_2)$ (eV)	$\Delta E(S_2-T_1)$ (eV)
<i>Uthrene-like compounds</i>							
2N-U	1.544 (2·10 ⁻⁴)	1.576 (0.007)	1.539	1.585	0.005	-0.009	0.037
2N2N-U_a	1.489 (0.001)	1.663 (0.160)	1.247	1.495	0.242	0.168	0.416
2N2N-U_b	1.421 (0.006)	1.557 (0.001)	1.410	1.509	0.011	0.048	0.147
2N4N-U	1.186 (0.004)	1.453 (0.065)	1.243	1.360	-0.057	0.093	0.210
12N-U	2.860 (0.021)	2.911 (0.015)	2.771	2.952	0.089	-0.041	0.140

2B-U	1.026 (0.002)	1.261 (0.002)	1.178	1.461	-0.152	-0.200	0.083
2B2N-U_a	1.537 (0.002)	1.617 (0.009)	1.582	1.615	-0.045	0.002	0.035
2B2N-U_b	1.514 (0.007)	1.719 (0.210)	1.543	1.598	-0.029	0.121	0.176
2B4N-U	1.841 ($3 \cdot 10^{-4}$)	1.852 ($8 \cdot 10^{-4}$)	1.942	1.984	-0.101	-0.132	-0.090
<i>Zethrene-like compounds</i>							
2N-Z	0.780 (0.007)	1.520 (0.000)	0.707	1.517	0.073	0.003	0.813
2N2N-Z_a	0.681 ($6 \cdot 10^{-4}$)	1.331 (0.000)	0.636	1.270	0.045	0.061	0.695
2N2N-Z_b	0.659 (0.001)	1.295 (0.000)	0.615	1.355	0.044	-0.060	0.680
2N4N-Z	0.563 (0.002)	1.093 (0.000)	0.561	1.241	0.002	-0.148	0.532
12N-Z	1.985 (0.144)	2.831 (0.000)	1.687	2.814	0.298	0.017	1.144
2B-Z	0.588 (0.000)	1.188 (0.000)	0.583	1.337	0.005	-0.149	0.605
2B2N-Z_a	0.805 (0.007)	1.511 (0.000)	0.751	1.626	0.054	-0.115	0.760
2B2N-Z_b	0.730 (0.005)	1.428 (0.000)	0.659	1.436	0.071	-0.008	0.769
2B4N-Z	1.006 (0.008)	1.778 (0.000)	0.873	1.863	0.133	-0.085	0.905

In line with the analysis carried out in the previous sections, the Uthrene-like compounds show higher S_1 and T_1 excitation energies than the Zethrene-like ones, consistently with their larger energy gap between the occupied and virtual orbitals involved in the main one-electron transition (see Tables S1 and S2). In contrast, S_2 and T_2 are described by a combination of one-electron transitions involving the four frontier MOs (Table S2). From Table S1, we observed that the energy gap between HOMO-1 and LUMO+1 is larger for the Zethrene-like compounds than for the Uthrene-like compounds. It follows that the combination of one-electron transitions dominating S_2 and T_2 balances the opposite trend characterizing the HOMO-LUMO and HOMO-1-LUMO+1 gap, explaining the weaker difference in S_2 and T_2 excitation energies between the two families.

Focusing now on the energy gap between excited states, Figure 5 shows the evolution of the S_1 - S_2 and T_1 - T_2 energy gaps for doped and undoped B- and N-centered Uthrene-like and Zethrene-like compounds. Overall, we observed that the singlet and the triplet excited states are lying closer to each other in Uthrene-like compared to Zethrene-like derivatives (see the average energy gap values indicated by the horizontal lines in Figure 5). In the Uthrene-like compounds, 2N-U and 2B-U show the smallest and the largest S_1 - S_2 and T_1 - T_2 energy differences, respectively (see Figure 5). The other Uthrene-like compounds exhibit intermediate values of the S_1 - S_2 and T_1 - T_2 energy gaps sometimes with large disparities in the magnitude of the two gaps as for the 2N4N-U compound. The Zethrene-like systems display a drastically different excited states picture, where the energy gap between the excited states with the same multiplicity ranges from 0.5 to nearly 1.2 eV, in any case larger than for Uthrene-like compounds. Consequently, a direct contribution coming from the S_2 and T_2 in the (R)ISC process is unlikely in Zethrene-like systems, leaving the direct S_1 - T_1 conversion as the sole active spin conversion path. Since S_1 and T_1 bear the same nature (see Table S2), the SOC between these two states should be small (El-Sayed's rule), leading to an expected low (R)ISC rate.

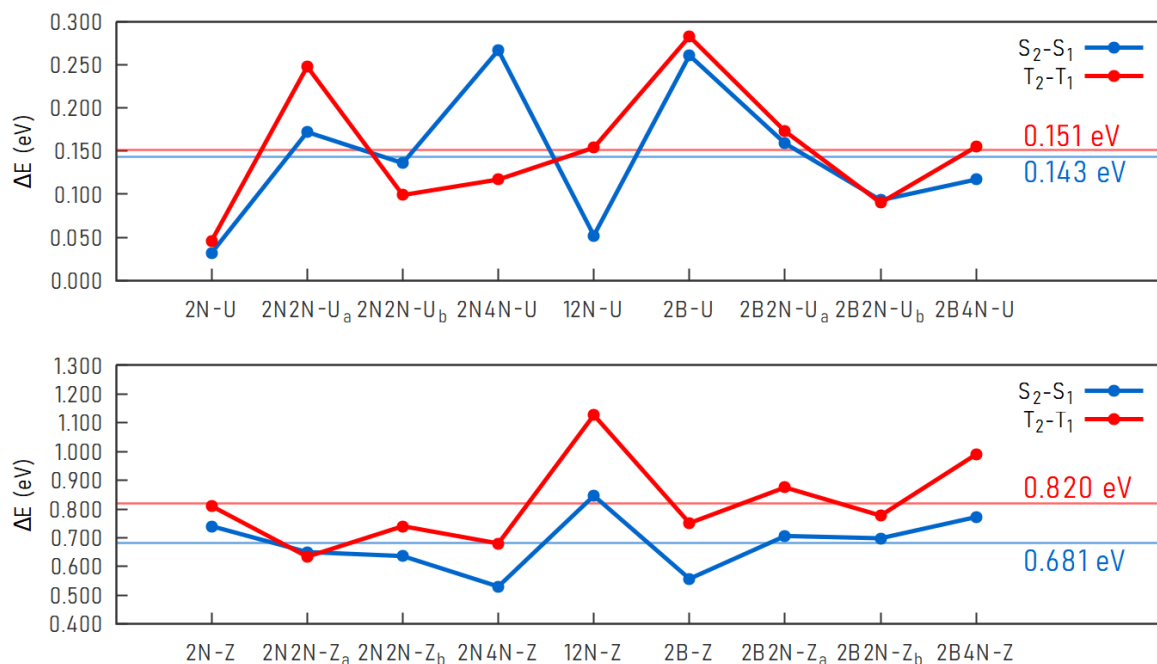


Figure 5: S_1 - S_2 and T_1 - T_2 energy gaps computed at NEVPT2(12,12)/def2-TZVP level of theory for the Uthrene-like (upper panel) and Zethrene-like (lower panel) systems at the ground state geometry. The horizontal lines define the energy gaps averaged over the respective set of Uthrene- and Zethrene-like systems.

Intriguingly, for both the Uthrene-like and Zethrene-like systems the S_1 - T_1 energy gap remains very small, in almost all the cases below 0.1 eV (see Table 3). In some instances, and especially in the case of boron-centered Uthrene-like compounds, the ΔE_{ST} becomes negative so that these molecules can be classified as X-INVEST. This can be related to the introduction of the N atoms on the vertices of the triangulene units that in this subset of compounds are atomic sites with a high HOMO density. It follows that the introduction of the more electronegative nitrogen atoms ensures a concentration of the HOMO density on these centers, reducing the exchange interaction and favoring the inversion. This suggests that the substitution of the central atoms in the triangulene units with boron atoms can be a valid strategy to achieve a negative S_1 - T_1 energy gap. Besides, all the Zethrene derivatives show a positive gap between S_1 and T_1 , even though it remains sufficiently small to leave possibilities for attempting substitutions driving the inversion.

The largest ΔE_{ST} observed for 2N2N-U_a, 2B4N-Z and 12N-Z range from roughly 0.1 to 0.3 eV (see Table 3) potentially still competitive to observe a TADF mechanism are obtained because of the contribution of different one-electron configurations to S_1 and T_1 (see Table S2). In 2N2N-U_a, the triplet excited state displaying the same nature as S_1 is T_2 , leading to negative S_1 - T_2 energy gaps. This inversion between singlet and triplet states bearing the same configuration that are not energetically consecutive is in line with what was observed in ref [28]. The same is valid for compound 12N-U (see Table S2), in which the small ΔE_{ST} (0.089 eV) and the non-negligible SOC arising from the different nature between S_1 and T_1 could have a strong impact on (R)ISC.

Moving to the S_2 - T_2 energy gap, for the Uthrene-like compounds, the trend associated with this energy gap parallels the one between S_1 - T_1 , *i.e.* molecules with a small or large (either positive or negative) value of the latter exhibit a small or large (either positive or negative) value of the former. For instance, 2B-U and 2B4N-U are predicted to have both large negative value of S_1 - T_1 gap (-0.152 eV and -0.101 eV, respectively) and S_2 - T_2 gap (-0.200 eV and -0.132 eV, respectively) while 2N2N-U_a display a large positive S_1 - T_1 and S_2 - T_2 gaps (see Table 3). The

remaining Uthrene-like compounds show both small S_1 - T_1 and S_2 - T_2 gaps, sometimes negative. A noteworthy case is 2B4N-U, where a negative gap is predicted between S_2 and T_1 (-0.090 eV), picturing an X-INVEST in which both the lowest singlet states lie below the lowest triplet state. This suggests that the extension process following the Uthrene symmetry starting from INVEST units, is a valid strategy to extend the energy inversion beyond the lowest singlet and triplet excited state. However, it consists in a necessary but not sufficient condition in view of some of the examples exhibiting positive energy gaps.

Interestingly, within the Zethrene family, all the compounds (except 12N-Z) show a negative gap between S_2 and T_2 in contrast with the trend in S_1 - T_1 gap. This inversion is rationalized through by evaluating the percentage of doubly excited configurations contributing to the excited states in the CASSCF wavefunction which exceeds 30% for all Zethrene compounds (except 12N-Z) much larger than in the case of Uthrene-like compounds where the percentage remains below 10%. In addition, the large energy gap between S_2 and T_1 (> 0.5 eV, see Table 4) makes unlikely its direct involvement in the RISC.

Figure 6 summarizes the possible energy order diagrams arising from the extended systems predicted by the NEVPT2(12,12) calculations at the ground state geometry:

- i) case **1-Z** obtained with the Zethrene-like structure with $\Delta E(S_1-T_1) > 0$ and $\Delta E(S_2-T_2) > 0$ (e.g. 2N-Z, 2N2N-Z_a and 12N-Z).
- ii) case **2-Z** obtained with the Zethrene-like structure with $\Delta E(S_1-T_1) > 0$ and $\Delta E(S_2-T_2) < 0$ (e.g. 2N2N-Z_b, 2N4N-Z, 2B-Z, 2B2N-Z_a, 2B2N-Z_b and 2B4N-Z).
- iii) case **1-U** obtained with the Uthrene-like structure with $\Delta E(S_1-T_1) > 0$ and $\Delta E(S_2-T_2) > 0$ (e.g. 2N2N-U_a and 2N2N-U_b).
- iv) case **2-U** obtained with the Uthrene-like structure with $\Delta E(S_1-T_1) < 0$ and $\Delta E(S_2-T_2) > 0$ (e.g. 2N4N-U, 2B2N-U_a and 2B2N-U_b).
- v) case **3-U** obtained with the Uthrene-like structure with $\Delta E(S_1-T_1) > 0$ and $\Delta E(S_2-T_2) < 0$ (e.g. 2N-U and 12N-U).
- vi) case **4-U** obtained with the Uthrene-like structure with $\Delta E(S_1-T_1) < 0$ and $\Delta E(S_2-T_2) < 0$ (e.g. 2B-U).
- vii) case **5-U** obtained with the Uthrene-like structure with $\Delta E(S_1-T_1) < 0$ and $\Delta E(S_2-T_2) < 0$ and $\Delta E(S_2-T_1) < 0$ (e.g. 2B4N-U).

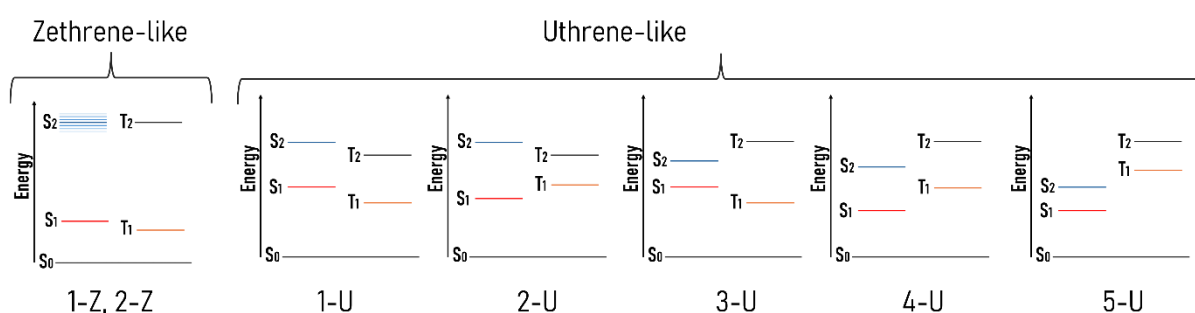


Figure 6: Different energy diagrams arising from the NEVPT2(12,12)/def2-TZVP calculations for the extended systems at the ground state geometry.

From Figure 6 it is clear that the parallel orientation is a promising strategy to design X-INVEST systems, where the energy proximity between singlet and triplet excited states, along with their inversion, can open new pathways for an efficient RISC and the population of the lowest singlet state (e.g. $T_1 \rightarrow S_2 \rightarrow S_1$, $T_2 \rightarrow S_1$, $T_2 \rightarrow S_2 \rightarrow S_1$). Besides, in the Zethrene-like architecture, the direct S_1 - T_1 path is the most likely spin conversion channel which, in view of the similar nature of the states, can hardly promote a fast RISC, with the S_2 and T_2 excited

states not being directly populated but potentially contributing to the process only through vibronic coupling. [49]

It is worth noting that the origin of these remarkable differences between the two extended triangulene families is a consequence of the different orientation at the connection between the single-core triangulene (section 3), showing how the molecular structure drives the photophysical properties of these systems.

6 Assessing the spin conversion dynamics of the Uthrene-like systems

In this section we will assess the role of the S_1 , T_1 , S_2 and T_2 excited states in the T_1 to S_1 conversion of Uthrene-like compounds only in view of their remarkable excited states features. Especially, we will focus on three candidates, belonging to the 1-U, 4-U and 5-U categories shown in Figure 6, the latter two representing X-INVEST systems. Unfortunately, for the Uthrene-like compounds belonging to the other categories, state swapping during the optimization of the excited states impeded reaching the equilibrium geometry of the correct states. To simulate the excited states dynamics, we integrated numerically a kinetic model including the rates of the different non-radiative elementary processes ((R)ISC, (reverse) internal conversion ((R)IC) taking place between these excited states to identify the contribution of these different pathways to the overall RISC process leading to the population of the S_1 state. In view of the prominent role played by the S_2 - S_1 IC processes in the two X-INVEST systems and their small energy gap, the respective rate constants calculated within the Fermi's Golden Rule framework have been validated against quantum dynamics simulations. The latter resort to an approach offering a remarkable trade-off between accuracy and computational cost (see Supporting Information for further details) and that recently has been employed by some of us for an efficient calculation of the IC rate in X-INVEST systems [55]. In order to mimic the spin-statistical population encountered in an OLED device, the initial population of the lowest singlet and triplet excited state were set to 0.25 and 0.75, respectively.

6.1 Geometry relaxation of the excited states

Figure 7 shows the energy scheme obtained upon the optimization of the four excited states in comparison with the Franck-Condon region (*i.e.* the ground state geometry). For 2N2N-U_b (Figure 7a), belonging to the 1-U scheme, *i.e.* $\Delta E(S_1-T_1)$ and $\Delta E(S_2-T_2)$ both > 0 at the ground state geometry, the energy order of scheme 1-U is retained, even though the energy spacing between the states is changed due to small but slightly different relaxations energies (see Table S9).

In the compound 2B-U (Figure 7b), which at the ground state geometry exhibits $\Delta E(S_1-T_1) < 0$ and $\Delta E(S_2-T_2) > 0$, thus belonging to the 4-U case, upon the relaxation of the excited state geometry, the S_2 state lies at lower energy than the T_1 state, leading to a negative adiabatic $\Delta E(S_2-T_1)$ energy gap, recalling the energy order of the scheme 5-U (Figure 6). Moreover, the larger relaxation of S_2 than S_1 (0.2 eV and 0.03 eV, respectively, see Table S9) leads the former to be located at lower energy than the latter in the adiabatic picture (Figure 7b), so that S_1 and S_2 exchange their nature from the Franck-Condon region to the adiabatic picture. However, the inclusion of the Zero Point Energy (ZPE) reverses again the energy order, with the two singlet states being quasi-degenerate ($\Delta E(S_2-S_1) = 0.016$ eV). Note that the relaxed geometry of the T_2 state is associated with an energy higher than the respective vertical one (Figure 7b and Table S9), artefact which might suggest that the geometry optimized at PBE0 level is not

consistent with an equilibrium geometry at NEVPT2 level. Nonetheless, the high energy of T_2 with respect to the other excited states leads its role to be negligible in the kinetic, thus we do not expect this inconsistency to be determinant (*vide infra*).

The 2B4N-U compound belongs to the 5-U case where both S_1 and S_2 lie below T_1 at the ground state geometry (Figure 6 and Table 4). As shown in Figure 7c, the geometry relaxation of the four excited states retains the same energy order found at the FC region, thus the 5-U scheme remains valid, with some changes in the energy gaps. However, the energy gaps involving the T_2 state are more affected because of its smaller reorganization energy (see Table S9). Therefore, a larger energy spacing is produced between T_2 and the other excited states upon relaxation, reducing its contribution to the overall RISC process. This is also corroborated by the significant small magnitude of the $S_1 \rightarrow T_2$ and $S_2 \rightarrow T_2$ ISC rates, despite the large value of the SOC assisting the former conversion (*vide infra*). Furthermore, the Reverse IC rate from T_1 to T_2 will be further decrease.

Overall, both 2B-U and 2B4N-U exhibit a negative adiabatic S_1-T_1 and S_2-T_2 and S_2-T_1 energy gap, thus consistently being X-INVEST systems when relaxing the geometries of the excited states.

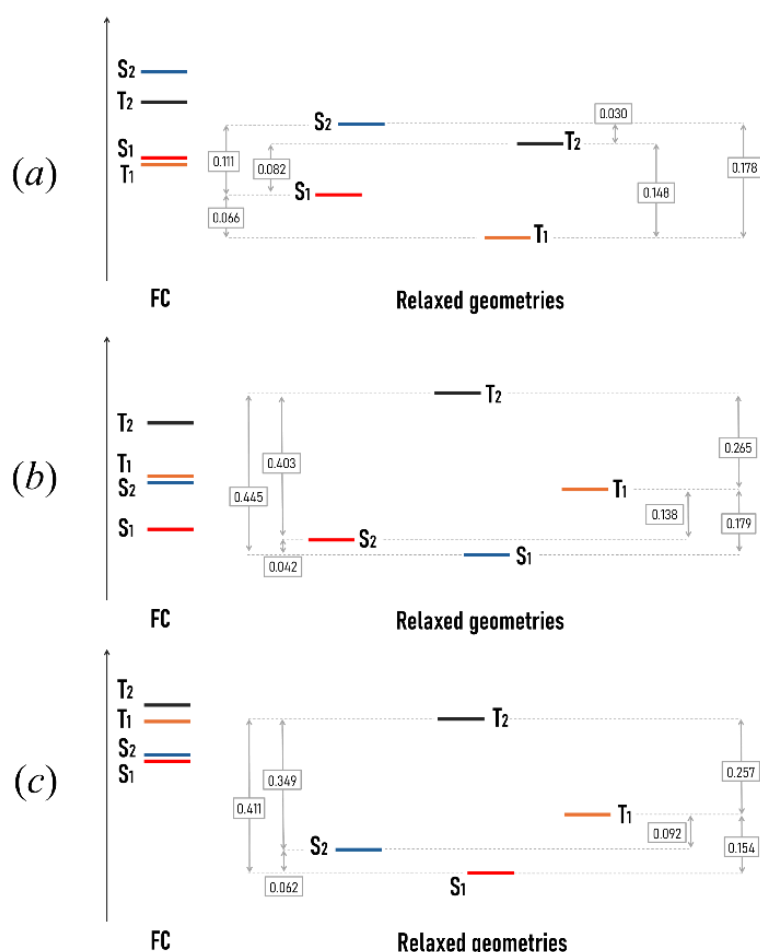


Figure 7: Energy diagram at the Franck-Condon (FC) and relaxed geometries of the excited states for 2N2N-U_b (a), 2B-U (b) and 2B4N-U (c) compounds. The ZPE correction is not included.

6.2 Radiative decay rates

Table 4 shows the values of the radiative decay rates for 2N2N-U_b, 2B-U and 2B4N-U evaluated within the Franck-Condon approximation and including the Herzberg-Teller corrections at the S₁ relaxed geometry (see S2 section for further details). The radiative rate constants have been calculated by using the following expression:

$$k_F = \frac{f_{osc}\Delta E^2}{1.499} \quad (1)$$

with ΔE the vertical excitation energy at S₁ geometry in cm⁻¹.

Table 4: Radiative rates calculated for 2N2N-U_b, 2B-U and 2B4N-U within the Franck-Condon and Herzberg-Teller approximation.

	k_F^{FC} (s ⁻¹)	k_F^{FC+HT} (s ⁻¹)
2N2N-U_b	$4.1 \cdot 10^5$	$8.0 \cdot 10^6$
2B-U	$4.2 \cdot 10^4$	$1.6 \cdot 10^6$
2B4N-U	$3.1 \cdot 10^4$	$1.2 \cdot 10^7$

As it can be seen, the inclusion of the Herzberg-Teller contribution leads to an increase of the radiative decay rates at least by one order of magnitude. In particular, for 2B4N-U, the fluorescence rate increased by three orders of magnitude.

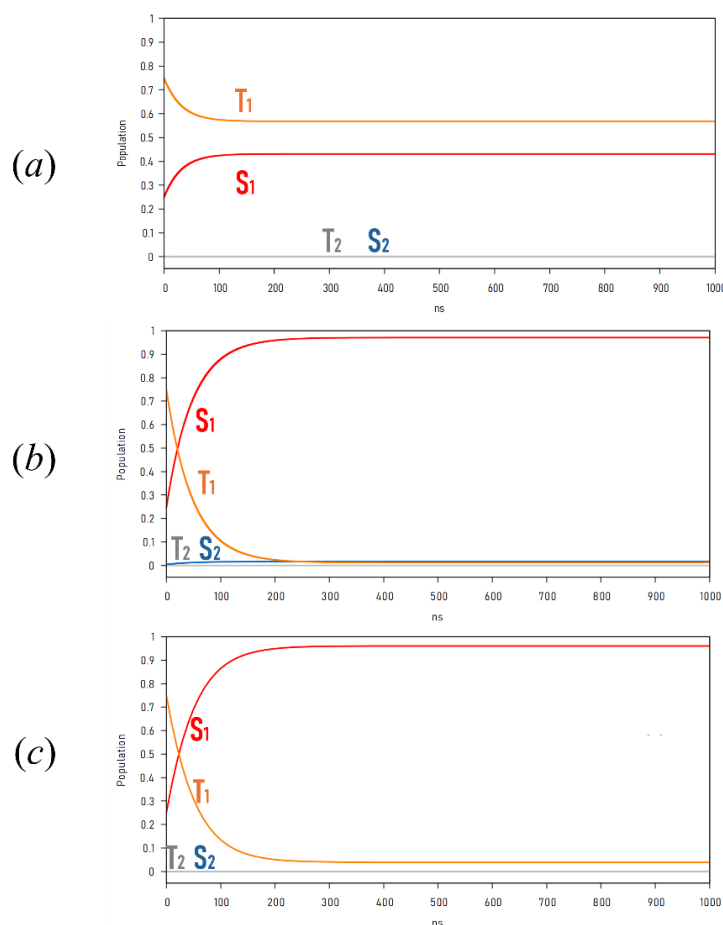


Figure 8: Excited state population as a function of time obtained by integrating the kinetic model for 2N2N-U_b (a), 2B-U (b) and 2B4N-U (c) compounds.

6.3 Spin conversion kinetics of 1-U case: 2N2N-U_b

Table 5 shows the SOC values computed between each singlet and triplet state. Even though S_1 and T_1 both receive the largest contribution from the HOMO \rightarrow LUMO transition at the ground state geometry (see Table S2), the SOC is different than zero. This originates from different excited configurations bearing a smaller weight that introduce differences in the nature between the two states. As a matter of fact, the third largest contribution in the S_1 and T_1 wavefunctions bears the same weight (≈ 0.02) but is associated with different electronic configurations, namely a HOMO,HOMO \rightarrow LUMO,LUMO transition for S_1 and a HOMO-1,HOMO \rightarrow LUMO,LUMO+2 transition, for T_1 . The same argument holds for the S_2 - T_2 SOC.

Interestingly, all the ISC processes exhibit a modestly large rate constants, the largest one being associated with the $S_1 \rightarrow T_1$ conversion, exploiting the largest SOC and its down-hill nature (Figure 7a). The smallest rate is associated with the $T_1 \rightarrow S_2$ conversion, which, despite the large SOC, is assisted by an up-hill process bearing the largest energy barrier (0.178 eV, Figure 7a). The IC rates have been computed for both the S_1 - S_2 and T_1 - T_2 conversions (see Table S10), with the forward ($S_2 \rightarrow S_1$ and $T_2 \rightarrow T_1$) processes largely outcompeting the backward ($S_1 \rightarrow S_2$ and $T_1 \rightarrow T_2$) ones.

Table 5: SOC values and ISC rate constants computed for the different spin conversion elementary processes of 2N2N-U_b. The SOC is associated with the value computed at the equilibrium geometry of the ground state.

	$S_1 \rightarrow T_1$	$T_1 \rightarrow S_1$	$S_1 \rightarrow T_2$	$T_2 \rightarrow S_1$	$S_2 \rightarrow T_1$	$T_1 \rightarrow S_2$	$S_2 \rightarrow T_2$	$T_2 \rightarrow S_2$
SOC (cm ⁻¹)	0.239		0.156		0.107		0.182	
k (s ⁻¹)	$2.2 \cdot 10^7$	$1.3 \cdot 10^7$	$1.5 \cdot 10^5$	$6.8 \cdot 10^6$	$1.6 \cdot 10^6$	$2.0 \cdot 10^2$	$1.4 \cdot 10^7$	$1.1 \cdot 10^7$

Figure 8a shows the population of the four excited states obtained through the integration of the kinetic equations within a time-window of 1000 ns. Interestingly, the population of S_1 increases within the first 100 ns, but remains constant after. T_1 population evolution perfectly mirrors the S_1 population variation. By fitting the S_1 population variation by employing a double exponential function, the initial population increase occurs with a rate of $3.3 \cdot 10^7$ s⁻¹, with the same order of magnitude as the $T_1 \rightarrow S_1$ RISC rate (Table 5). Interestingly, T_2 and S_2 populations remain close to zero during the entire time interval. However, it is not necessarily clear whether the S_2 and T_2 are populated and depopulated almost instantaneously. To uncover this aspect, we simulated the spin conversion dynamics by systematically removing the elementary processes involving S_2 and T_2 (both ISC and RISC) from the kinetic (see Figure S6 for the population variation). As it can be seen, the magnitude of the rate associated with the growth of S_1 population retains the same value in all the simulations. Specifically, by removing both the S_1 - T_2 and S_2 - T_1 conversion channels, the population of S_1 increases at the same rate as the one obtained by including all the processes (see Table 6). This is due to the larger IC rates that outcompete the Reverse-IC (RIC), allowing a fast depopulation of the two higher-lying excited states, resulting in their negligible contribution to the S_1 population. It follows that for 2N2N-U_b, the sole channel active in the overall RISC is the direct S_1 - T_1 conversion.

Table 6: S_1 population rates resulting from the fitting as a function of the included elementary processes.

	All processes	No S_1 - T_2	No S_2 - T_1	No S_1 - T_2 and S_2 - T_1
$k [S_1]$ (s ⁻¹)	$3.3 \cdot 10^7$	$3.3 \cdot 10^7$	$3.3 \cdot 10^7$	$3.3 \cdot 10^7$

6.4 Spin conversion kinetics of 4-U case: 2B-U

The SOC value between the T_1 and S_2 states appears to be the largest one, so that the largest ISC and RISC rates (up to 10^7 s^{-1} , see Table 7) involve these two states. The ISC rates involving the T_2 state (*i.e.* $S_1 \rightarrow T_2$ and $S_2 \rightarrow T_2$) are somewhat smaller due to a combination of smaller SOC and larger energy gap between the states (see Figure 7b and Table 7). However, the main limitation to a spin conversion mechanism through T_2 is the largely unbalanced $T_2 \rightarrow T_1$ IC and $T_1 \rightarrow T_2$ RIC rates ($2.3 \cdot 10^{15} \text{ s}^{-1}$ and $1.5 \cdot 10^9 \text{ s}^{-1}$, respectively), the latter process being the only process able to result in a significant T_2 population.

Table 7: SOC values and ISC rate constants computed for the different spin conversion elementary processes of 2B-U. The SOC is associated with the value computed at the equilibrium geometry of the initial state.

	$S_1 \rightarrow T_1$	$T_1 \rightarrow S_1$	$S_1 \rightarrow T_2$	$T_2 \rightarrow S_1$	$S_2 \rightarrow T_1$	$T_1 \rightarrow S_2$	$S_2 \rightarrow T_2$	$T_2 \rightarrow S_2$
SOC (cm^{-1})	0.006		0.146		0.299		0.006	
k (s^{-1})	$1.6 \cdot 10^4$	$1.7 \cdot 10^4$	$3.4 \cdot 10^1$	$2.7 \cdot 10^6$	$1.3 \cdot 10^7$	$2.1 \cdot 10^7$	$2.3 \cdot 10^{-1}$	$9.5 \cdot 10^2$

In Figure 8b, a fast population of the S_1 state is observed after 200 ns, while the population of T_1 follows the same but opposite trend. By fitting the S_1 population variation with a biexponential function, the resulting rate of increase of the S_1 population turned out to be $2.1 \cdot 10^7 \text{ s}^{-1}$ (see Table 8). This reflects the $T_1 \rightarrow S_2$ RISC, which represents the rate limiting process to reach the S_1 state since the $S_2 \rightarrow S_1$ IC is extremely fast ($8.0 \cdot 10^{13} \text{ s}^{-1}$). We mention here that the extremely fast $S_2 \rightarrow S_1$ IC rate computed within the Fermi's Golden rule (FGR) has been validated against quantum dynamics calculations resulting in this case to an IC rate of $6.6 \cdot 10^{13} \text{ s}^{-1}$ (see Supporting Information for more details).

When solving the kinetic model neglecting the T_1 - S_2 channel, we observed no variation of the S_1 and T_1 excited state population with respect to the initial condition (see Table 8 and Figure S7b), which confirmed the crucial role of the $T_1 \rightarrow S_2$ RISC process. Neglecting the involvement of the T_2 state does not change the rate of the overall spin conversion process (see Table 7 and Figure S5a). Furthermore, by blocking the S_1 - T_1 channel and allowing the $S_2 \rightarrow S_1$ IC to be the sole source of S_1 population, the latter state is again populated with the initial large rate of $2.1 \cdot 10^7 \text{ s}^{-1}$ (see Figure 9a). On the contrary, by blocking the S_1 - S_2 pathway, the high $T_1 \rightarrow S_2$ rate largely outcompetes the one associated with the $T_1 \rightarrow S_1$ conversion, hampering the population of S_1 but promoting an increase in the S_2 population (see Figure 9b).

Table 8: S_1 population rates resulting from the fitting as a function of the included elementary processes for 2B-U.

	All processes	No S_1 - T_2	No S_2 - T_1	No S_1 - T_2 and S_2 - T_1
$k [S_1]$ (s^{-1})	$2.1 \cdot 10^7$	$2.1 \cdot 10^7$	No variation	No variation

It follows that the S_2 state plays a determinant role in the spin conversion of 2B-U, with the $T_1 \rightarrow S_2 \rightarrow S_1$ process allowing for the fast population of the lowest singlet excited state.

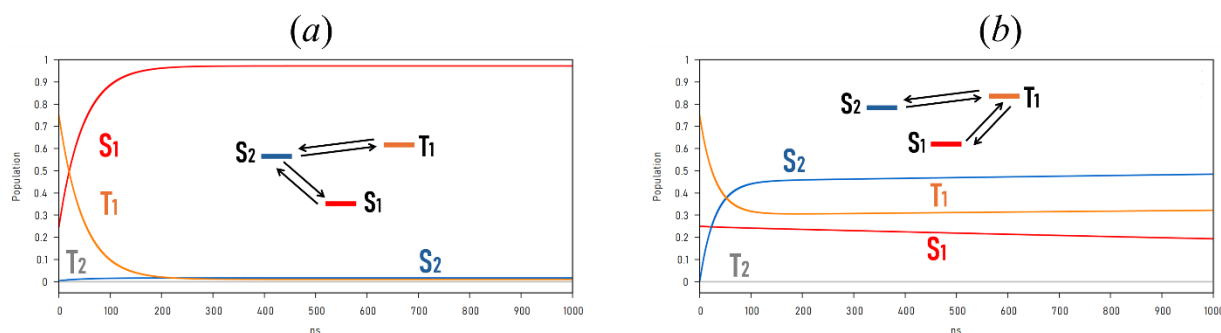


Figure 9: Population variation of the four excited states. (a) Kinetic obtained by neglecting the S_1 - T_1 IC channel; (b) kinetic obtained by neglecting the S_1 - S_2 ISC channel for 2B-U.

6.5 Spin conversion kinetics of 5-U case: 2B4N-U

As shown in Table 9, the largest SOC values are obtained between S_2 and T_1 , by virtue of the different nature characterizing these two states, that is a combination of HOMO \rightarrow LUMO+1 and HOMO-1 \rightarrow LUMO for the former and the sole HOMO \rightarrow LUMO for the latter. It is worth noticing that the $S_2\rightarrow T_1$ ISC is faster by one order of magnitude than the $T_1\rightarrow S_2$ one since the introduction of the ZPE correction leads the S_2 - T_1 energy gap to be positive (contrarily to the sole adiabatic energy gap, Figure 7c), even though very small (0.016 eV), thus driving the former conversion through an up-hill pathway. The resulting IC rates turned out to be as high as $1.0\cdot 10^{15}\text{ s}^{-1}$ and $5.0\cdot 10^{10}\text{ s}^{-1}$ for the $S_2\rightarrow S_1$ and the $S_1\rightarrow S_2$ conversion, respectively, thanks to the small adiabatic energy gap between the two singlet states (0.062 eV). In light of the very high value of the $S_2\rightarrow S_1$ rate, which could be outside the range of validity of FGR,[55] we have checked through quantum dynamics calculations the rate value for both IC and RIC processes. Our simulations (see Supporting Information) revealed a rate of $3.1\cdot 10^{14}$ and $8.1\cdot 10^9$ for the $S_2\rightarrow S_1$ and the $S_1\rightarrow S_2$ conversions, respectively, in fair agreement with the FGR values. The agreement for both 2B-U and 2B4N-U molecules indicates that using the computationally less expensive FGR approach is justified and does not compromise the accuracy of our analysis.

Table 9: SOC values and ISC rate constants computed for the different spin conversion elementary processes of 2B4N-U. The SOC is associated with the value computed at the equilibrium geometry of the initial state.

	$S_1\rightarrow T_1$	$T_1\rightarrow S_1$	$S_1\rightarrow T_2$	$T_2\rightarrow S_1$	$S_2\rightarrow T_1$	$T_1\rightarrow S_2$	$S_2\rightarrow T_2$	$T_2\rightarrow S_2$
SOC (cm^{-1})	0.083		0.166		0.459		0.102	
k (s^{-1})	$8.4\cdot 10^5$	$2.2\cdot 10^6$	5.84	$5.4\cdot 10^6$	$3.6\cdot 10^7$	$1.4\cdot 10^7$	$6.9\cdot 10^2$	$1.8\cdot 10^6$

Figure 8c shows that the population variation of the four excited states occurs in a time-window of 300 ns. As can be seen, S_1 and T_1 exhibit the most prominent population variation among the four states, with the S_2 and T_2 states remaining close to zero throughout the entire simulation. This is consistent with the outcompeting ultrafast rates of the forward-IC process, impeding a significant population of the latter two states. The double exponential fitting provides $1.9\cdot 10^7\text{ s}^{-1}$ as the fastest rate of the S_1 population increasing, similar order of magnitude of the S_2 - T_1 elementary (R)ISC rate (see Table 9). As shown in Table 10 and Figure S8, the contribution of the S_1 - T_2 channel is confirmed to be irrelevant in the overall RISC process, with a resulting S_1 population rate when neglecting this channel equal to the one obtained including all the process. On the contrary, by neglecting the S_2 - T_1 channel the S_1 population rate results to be $2.3\cdot 10^6\text{ s}^{-1}$, one order of magnitude smaller than the one obtained

with its inclusion, suggesting that the main spin conversion path involves the S₂-T₂ channel. It follows that this spin conversion channel plays a non-negligible role in the total spin conversion process.

Table 10: S₁ population rates resulting from the fitting as a function of the included elementary processes for 2B4N-U.

	All processes	No S ₁ -T ₂	No S ₂ -T ₁	No S ₁ -T ₂ and S ₂ -T ₁
$k [S_1] (s^{-1})$	$1.9 \cdot 10^7$	$1.9 \cdot 10^7$	$3.3 \cdot 10^6$	$2.3 \cdot 10^6$

To disclose the role of the pathways involving the S₂ state we simulated the kinetic of two possible scenarios: (i) neglecting the S₁-S₂ IC, thus leaving active only the S₂-T₁ and the S₁-T₁ channels (Figure 10a) and (ii) neglecting the S₁-T₁ ISC, thus leaving active only the S₁-S₂ and S₂-T₁ pathways (Figure 10b).

By neglecting the S₁-S₂ IC, the sole source of population of S₁ is T₁, the latter undergoing the ISC with the two singlets. As shown in Figure 10a, the S₂ exhibits an increase in its population reaching a maximum of 0.2 within the first 100 ns, reflecting the sudden decrease in T₁ population occurring within the same time range. On the contrary, the S₁ population slowly increases, reaching a steady value of 0.78, with a rate of $2.3 \cdot 10^6 s^{-1}$, one order of magnitude lower than the total rate predicted by including all the processes. It follows that cutting off the S₁-S₂ channel is detrimental for the spin conversion dynamics.

In the other scenario, the source of S₁ population derives from the S₁-S₂ IC path. As shown in Figure 10b, the S₁ kinetic is significantly faster than the previous case, with an overall rate equal to $1.0 \cdot 10^7 s^{-1}$, thus allowing recovering similar S₁ population increase rate (see Table 10). Consequently, the S₂ state plays a crucial role in determining an efficient RISC process. Specifically, despite the comparable rate associated with the T₁→S₂ and S₂→T₁ conversion, the ultrafast S₂→S₁ IC impedes the realization of an equilibrium between the former states, behaving as a funnel for the population of the S₁ state.

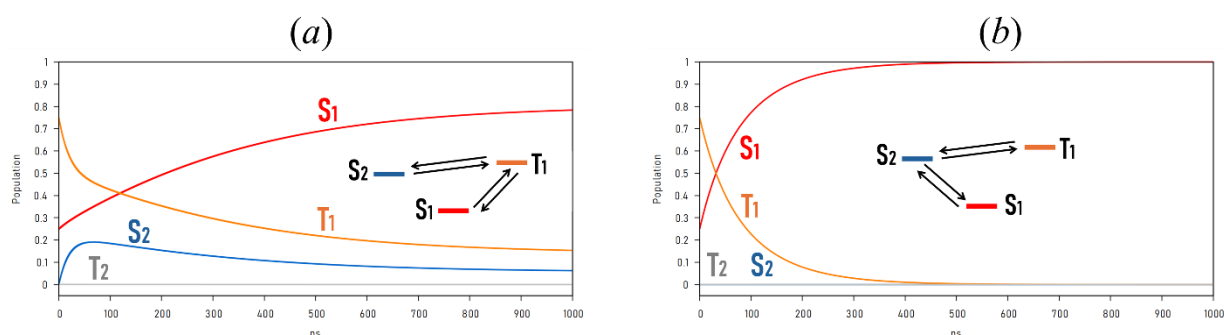


Figure 10: Population variation of the four excited states. (a) Kinetic obtained by neglecting the S₁-S₂ IC channel; (b) kinetic obtained by neglecting the S₁-T₁ ISC channel for 2B4N-U.

To establish a more comprehensive picture of the spin conversion dynamics of 2B-U and 2B4N-U, we extended the kinetic model by including the irreversible S₁ → S₀ radiative decay employing the fluorescence rate constants computed including the Herzberg-Teller corrections (see Table 4). Figure 11a and Figure 11b show the ground and excited state population variations for 2B-U and 2B4N-U, respectively. In both cases, a fast increase in S₁ population occurs within ≈100 ns followed by a decrease mirroring the increase in the ground state population (see Figure 11). By fitting the ground state population variation employing a double exponential function, its population turned out to occur with a rate of $2.3 \cdot 10^6 s^{-1}$ and $8.9 \cdot 10^6 s^{-1}$ for 2B-U (Figure 11a) and 2B4N-U (Figure 11b), respectively.

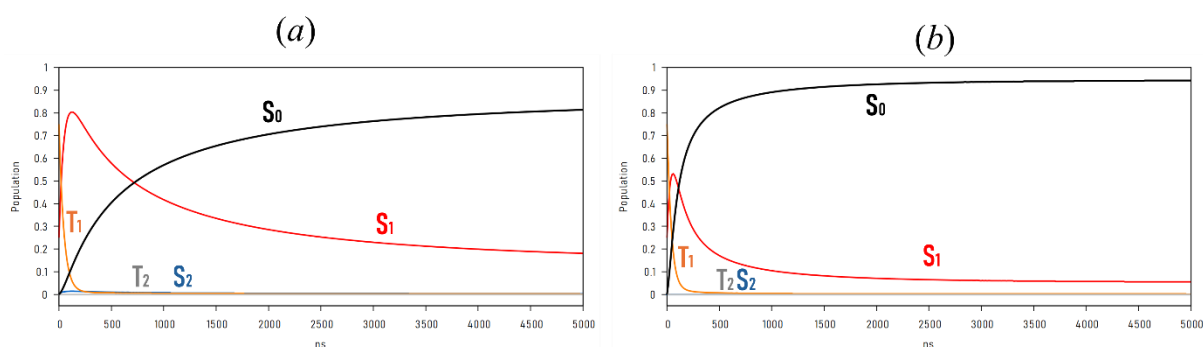


Figure 11: Population variation of ground and excited states for 2B-U (a) and 2B4N-U (b) compounds.

7 Conclusions

In this work, we designed a series of extended triangulene systems, doped with N and B atoms, and assessed their excitation energies employing wavefunction-based methods. In addition, we simulated the rate constants of radiative and non-radiative decay processes from *first principle* formalisms.

The extension strategy entailed the connection of two INVEST single-core triangulenes according to a parallel and an antiparallel orientation, resulting in Uthrene- and Zethrene-like structures, respectively. The calculations and the simulations carried out on these systems allowed discerning useful information from both a computational and a molecular design perspective:

- *Electronic structure methods performance:* EOM-CCSD and NEVPT2(12,12) were benchmarked on two reference extended compounds, namely 2N-U and 2N-Z. While it overestimates the singlet excitation energies for Zethrene-like molecules, the main issues with EOM-CCSD comes from the poor description of the S_2 excited states due to the large double excitation character. For this reason, NEVPT2(12,12) was identified as a method able to predict accurately energy gaps between the S_1 , S_2 , T_1 and T_2 excited states.
- *Singlet-triplet energy gaps:* the NEVPT2 calculations carried out on the Uthrene- and Zethrene-like molecules revealed that in both cases small S_1 - T_1 and S_2 - T_2 energy gaps can be achieved, with the largest values ≈ 0.2 eV. Specifically, in some Uthrene-like systems, in particular the B-centered ones, the singlet-triplet energy gaps acquired negative values, thus effectively representing X-INVEST systems. More intriguingly, in 2B-4N-U both S_1 and S_2 lie below T_1 . In the Zethrene-like compounds, the S_1 - T_1 is systematically predicted to be small but always positive. On the contrary, for some of these compounds the S_2 - T_2 energy gap acquired negative values, behavior due to the large presence of double excitations in the S_2 wavefunction ($> 50\%$), leading to a significant contribution of electron correlation effects stabilizing the singlet state with respect to the triplet counterpart.
- *S_1 - S_2 and T_1 - T_2 energy gaps:* NEVPT2 calculations systematically predicted small energy gaps between S_1 - S_2 and T_1 - T_2 for the Uthrene- while large energy gaps are

obtained Zethrene-like compounds, respectively. A careful inspection of the MOs distribution of the extended structures showed that the parallel orientation promotes the *non-bonding* character in the four frontier MOs, inducing small HOMO-HOMO-1 and LUMO+1-LUMO energy gaps in the Uthrene-like systems. On the contrary, the antiparallel orientation only leads to the formation of *bonding* and *anti-bonding* MOs, consequently determining large HOMO-HOMO-1 and LUMO+1-LUMO energy gaps in the Zethrene-like systems. This translates in the small and large energy difference between the S₁-S₂ and the T₁-T₂ excited states for the Uthrene- and Zethrene-like compounds, respectively, whose excited states wavefunctions receive dominant contributions from transitions between these four frontier MOs.

- (*R*)ISC process: the small singlet-triplet energy gaps found for both the Uthrene-like and Zethrene-like systems make these compounds promising candidates for a fast spin conversion. However, the similar S₁ and T₁ nature precludes a fast (R)ISC involving these two states (El-Sayed's rules), consequently requiring the involvement of higher-lying excited states mediating the spin conversion. In the Zethrene-like systems, the large energy gap between S₁ and T₁ and the higher lying excited states impedes a direct mediation by the latter, making their contribution possible only through vibronic coupling mechanisms (*e.g.* Herzberg-Teller or Spin-Vibronic Coupling effects). On the contrary, the energy proximity established between the S₁, T₁, S₂ and T₂ in the Uthrene-like systems opens new alternative pathways involving all the four excited states. To corroborate this hypothesis, we computed the (R)ISC rates and simulated the spin conversion kinetics for three Uthrene-like systems, namely 2N2N-U_b, 2B-U and 2B-4N-U. While in the first one the spin conversion process is driven by a direct S₁-T₁ (R)ISC, in both the X-INVEST 2B-U and 2B-4N-U compounds the T₁-S₂ channel turned out to be the fastest, thanks to the energy resonance reached between the two excited states. Specifically, our simulations showed that in these compounds the RISC occurs through a two-step process, involving a fast T₁ → S₂ conversion followed by an ultrafast S₂ → S₁ internal conversion, with the S₂ behaving as a funnel for the population of S₁, a process occurring with a rate of $\approx 10^7$ s⁻¹.

In conclusion, in this work we showed how the symmetry adopted in the connection process of triangulene units can dictate the electronic and photophysical properties of the final extended triangulene systems. In particular, the parallel orientation represents a fruitful design strategy to build X-INVEST cores, in which the energy proximity between the lowest singlet and triplet excited states can pave the way to a new paradigm for a fast RISC mechanism.

Acknowledgement

Y.O. acknowledges funding by the Fonds de la Recherche Scientifique-FNRS under Grant n° F.4534.21 (MIS-IMAGINE). G. R. acknowledges a grant from the “Fonds pour la formation a la Recherche dans l’Industrie et dans l’Agriculture” (FRIA) of the FRS-FNRS. Computational resources were also provided by the “Consortium des Équipements de Calcul Intensif” (CÉCI), funded by the “Fonds de la Recherche Scientifiques de Belgique” (FRS-FNRS) under Grant No. 2.5020.11. A.L. gratefully acknowledges funding from the Italian Ministry of University and Research (MUR, PRIN grant 2022XSC9P5).

References

- [1] Hund, F., *Linienspektren und Periodisches System der Elemente*, Springer Vienna 1927.
- [2] Adachi, C., 2014. Third-generation organic electroluminescence materials. *Jpn. J. Appl. Phys.* 53, 06010.
- [3] Shi, Y.-Z., Wu, H., Wang, K., Yu, J., Ou, X.-M., Zhang, X.-H., 2022. Recent progress in thermally activated delayed fluorescence emitters for nondoped organic light-emitting diodes. *Chem. Sci.* 13, 3625–3651.
- [4] Uoyama, H., Goushi, K., Shizu, K., Nomura, H., Adachi, C., 2012. Highly efficient organic light-emitting diodes from delayed fluorescence. *Nature* 492, 234–238.
- [5] Endo, A., Sato, K., Yoshimura, K., Kai, T., Kawada, A., Miyazaki, H., Adachi, C., 2011. Efficient up-conversion of triplet excitons into a singlet state and its application for organic light emitting diodes. *Applied Physics Letters* 98, 083302.
- [6] Hatakeyama, T., Shiren, K., Nakajima, K., Nomura, S., Nakatsuka, S., Kinoshita, K., Ni, J., Ono, Y., Ikuta, T., 2016. Ultrapure Blue Thermally Activated Delayed Fluorescence Molecules: Efficient HOMO–LUMO Separation by the Multiple Resonance Effect. *Advanced Materials* 28, 2777–2781.
- [7] Pershin, A., Hall, D., Lemaire, V., Sancho-Garcia, J.-C., Muccioli, L., Zysman-Colman, E., Beljonne, D., Olivier, Y., 2019. Highly emissive excitons with reduced exchange energy in thermally activated delayed fluorescent molecules. *Nat Commun* 10, 597.
- [8] Kondo, Y., Yoshiura, K., Kitera, S., Nishi, H., Oda, S., Gotoh, H., Sasada, Y., Yanai, M., Hatakeyama, T., 2019. Narrowband deep-blue organic light-emitting diode featuring an organoboron-based emitter. *Nat. Photonics* 13, 678–682.
- [9] S. Oda, B. Kawakami, M. Horiuchi, Y. Yamasaki, R. Kawasumi, T. Hatakeyama, Ultra-Narrowband Blue Multi-Resonance Thermally Activated Delayed Fluorescence Materials. *Adv. Sci.* 2022, 10, 2205070.
- [10] Pu, Y.-J., Valverde, D., Sancho-García, J.C., Olivier, Y., 2023. Computational Design of Multiple Resonance-Type BN Molecules for Inverted Singlet and Triplet Excited States. *J. Phys. Chem. A* 127, 10189–10196.

- [11] Aizawa, N., Pu, Y.J., Harabuchi, Y. et al. Delayed fluorescence from inverted singlet and triplet excited states. *Nature* 609, 502–506 (2022).
- [12] Leupin, W., Wirz, J., 1980. Low-lying electronically excited states of cycl[3.3.3]azine, a bridged 12.πi-perimeter. *J. Am. Chem. Soc.* 102, 6068–6075.
- [13] Leupin, Werner., Magde, Douglas., Persy, Gabriele., Wirz, Jakob., 1986. 1,4,7-Triazacycl[3.3.3]azine: basicity, photoelectron spectrum, photophysical properties. *J. Am. Chem. Soc.* 108, 17–22.
- [14] Ehrmaier, J., Rabe, E.J., Pristash, S.R., Corp, K.L., Schlenker, C.W., Sobolewski, A.L., Domcke, W., 2019. Singlet–Triplet Inversion in Heptazine and in Polymeric Carbon Nitrides. *J. Phys. Chem. A* 123, 8099–8108.
- [15] Ehrmaier, J., Karsili, T.N.V., Sobolewski, A.L., Domcke, W., 2017. Mechanism of Photocatalytic Water Splitting with Graphitic Carbon Nitride: Photochemistry of the Heptazine–Water Complex. *J. Phys. Chem. A* 121, 4754–4764.
- [16] Chen, D., Chen, Weiben, Zhang, G., Li, S., Chen, Weihua, Xing, G., Chen, L., 2022. N-Rich 2D Heptazine Covalent Organic Frameworks as Efficient Metal-Free Photocatalysts. *ACS Catal.* 12, 616–623.
- [17] Domcke, W., Sobolewski, A.L., Schlenker, C.W., 2020. Photooxidation of water with heptazine-based molecular photocatalysts: Insights from spectroscopy and computational chemistry. *The Journal of Chemical Physics* 153, 100902.
- [18] De Silva, P., 2019. Inverted Singlet–Triplet Gaps and Their Relevance to Thermally Activated Delayed Fluorescence. *J. Phys. Chem. Lett.* 10, 5674–5679.
- [19] G. Ricci, E. San-Fabián, Y. Olivier, J. C. Sancho-García, Singlet-Triplet Excited-State Inversion in Heptazine and Related Molecules: Assessment of TD-DFT and ab initio Methods *ChemPhysChem* 2021, 22, 553.
- [20] Sanz-Rodrigo, J., Ricci, G., Olivier, Y., Sancho-García, J.C., 2021. Negative Singlet–Triplet Excitation Energy Gap in Triangle-Shaped Molecular Emitters for Efficient Triplet Harvesting. *J. Phys. Chem. A* 125, 513–522.
- [21] Loos, P.-F., Lipparini, F., Jacquemin, D., 2023. Heptazine, Cyclazine, and Related Compounds: Chemically-Accurate Estimates of the Inverted Singlet–Triplet Gap. *J. Phys. Chem. Lett.*
- [22] Dreuw, A., Hoffmann, M., 2023. The inverted singlet–triplet gap: a vanishing myth? *Front. Chem.* 11, 1239604.
- [23] Bedogni, M., Giavazzi, D., Di Maiolo, F., Painelli, A., 2024. Shining Light on Inverted Singlet–Triplet Emitters. *J. Chem. Theory Comput.* 20, 902–913.
- [24] Ricci, G., Sancho-García, J.-C., Olivier, Y., 2022. Establishing design strategies for emissive materials with an inverted singlet–triplet energy gap (INVEST): a computational perspective on how symmetry rules the interplay between triplet harvesting and light emission. *J. Mater. Chem. C* 10, 12680–12698.

- [25] Pollice, R., Friederich, P., Lavigne, C., Gomes, G.D.P., Aspuru-Guzik, A., 2021. Organic molecules with inverted gaps between first excited singlet and triplet states and appreciable fluorescence rates. *Matter* 4, 1654–1682.
- [26] Robert Pollice, Benjamin Ding, Alán Aspuru-Guzik, Rational design of organic molecules with inverted gaps between the first excited singlet and triplet, *Matter*, 2024, ISSN 2590-2385.
- [27] Omar, Ö.H., Xie, X., Troisi, A., Padula, D., 2023. Identification of Unknown Inverted Singlet–Triplet Cores by High-Throughput Virtual Screening. *J. Am. Chem. Soc.* 145, 19790–19799.
- [28] J. Terence Blaskovits, M. H. Garner, C. Corminboeuf, Symmetry-Induced Singlet-Triplet Inversions in Non-Alternant Hydrocarbons *Angew. Chem. Int. Ed.* 2023, 62, e202218156; *Angew. Chem.* 2023, 135.
- [29] Garner, M.H., Blaskovits, J.T., Corminboeuf, C., Enhanced inverted singlet–triplet gaps in azaphenalenenes and non-alternant hydrocarbons. *Chem. Commun.*, 2024, 60, 2070.
- [30] Shizu, K., Kaji, H., 2022. Comprehensive understanding of multiple resonance thermally activated delayed fluorescence through quantum chemistry calculations. *Commun Chem* 5, 53.
- [31] Marian, C.M., 2021. Understanding and Controlling Intersystem Crossing in Molecules. *Annu. Rev. Phys. Chem.* 72, 617–640.
- [32] Dinkelbach, F., Bracker, M., Kleinschmidt, M., Marian, C.M., 2021. Large Inverted Singlet–Triplet Energy Gaps Are Not Always Favorable for Triplet Harvesting: Vibronic Coupling Drives the (Reverse) Intersystem Crossing in Heptazine Derivatives. *J. Phys. Chem. A* 125, 10044–10051.
- [33] Sobolewski, A.L., Domcke, W., 2023. Excited-state singlet–triplet inversion in hexagonal aromatic and heteroaromatic compounds. *Phys. Chem. Chem. Phys.* 25, 21875–21882.
- [34] Melle-Franco, M., 2015. Uthrene, a radically new molecule? *Chem. Commun.* 51, 5387–5390.
- [35] Grimme, S., 2003. Improved second-order Møller–Plesset perturbation theory by separate scaling of parallel- and antiparallel-spin pair correlation energies. *The Journal of Chemical Physics* 118, 9095–9102.
- [36] Christiansen, O., Koch, H., Jørgensen, P., 1995. The second-order approximate coupled cluster singles and doubles model CC2. *Chemical Physics Letters* 243, 409–418.
- [37] Stanton, J.F., Bartlett, R.J., 1993. The equation of motion coupled-cluster method. A systematic biorthogonal approach to molecular excitation energies, transition probabilities, and excited state properties. *The Journal of Chemical Physics* 98, 7029–7039.
- [38] B. Roos, A new method for large-scale CI calculations, *Chemical Physics Letters*, Volume 15, Issue 2, 1972, 153-159.
- [39] Angeli, C., Cimiraglia, R., Malrieu, J.-P., 2001. N-electron valence state perturbation theory: a fast implementation of the strongly contracted variant. *Chemical Physics Letters* 350, 297–305.

[40] TURBOMOLE V7.4.1 2019, a development of University of Karlsruhe and Forschungszentrum Karlsruhe GmbH, 1989-2007, TURBOMOLE GmbH, since 2007; available from <http://www.turbomole.com>.

[41] Epifanovsky, E., Gilbert, A.T.B., Feng, X., Lee, J., Mao, Y., Mardirossian, N., Pokhilko, P., White, A.F., Coons, M.P., Dempwolff, A.L., Gan, Z., Hait, D., Horn, P.R., Jacobson, L.D., Kaliman, I., Kussmann, J., Lange, A.W., Lao, K.U., Levine, D.S., Liu, J., McKenzie, S.C., Morrison, A.F., Nanda, K.D., Plasser, F., Rehn, D.R., Vidal, M.L., You, Z.-Q., Zhu, Y., Alam, B., Albrecht, B.J., Aldossary, A., Alguire, E., Andersen, J.H., Athavale, V., Barton, D., Begam, K., Behn, A., Bellonzi, N., Bernard, Y.A., Berquist, E.J., Burton, H.G.A., Carreras, A., Carter-Fenk, K., Chakraborty, R., Chien, A.D., Closser, K.D., Cofer-Shabica, V., Dasgupta, S., de Wergifosse, M., Deng, J., Diedenhofen, M., Do, H., Ehlert, S., Fang, P.-T., Fatehi, S., Feng, Q., Friedhoff, T., Gayvert, J., Ge, Q., Gidofalvi, G., Goldey, M., Gomes, J., González-Espinoza, C.E., Gulania, S., Gunina, A.O., Hanson-Heine, M.W.D., Harbach, P.H.P., Hauser, A., Herbst, M.F., Hernández Vera, M., Hodecker, M., Holden, Z.C., Houck, S., Huang, X., Hui, K., Huynh, B.C., Ivanov, M., Jász, Á., Ji, H., Jiang, H., Kaduk, B., Kähler, S., Khistyayev, K., Kim, J., Kis, G., Klunzinger, P., Koczor-Benda, Z., Koh, J.H., Kosenkov, D., Koulias, L., Kowalczyk, T., Krauter, C.M., Kue, K., Kunitsa, A., Kus, T., Ladjánszki, I., Landau, A., Lawler, K.V., Lefrançois, D., Lehtola, S., Li, R.R., Li, Y.-P., Liang, J., Liebenthal, M., Lin, H.-H., Lin, Y.-S., Liu, F., Liu, K.-Y., Loipersberger, M., Luenser, A., Manjanath, A., Manohar, P., Mansoor, E., Manzer, S.F., Mao, S.-P., Marenich, A.V., Markovich, T., Mason, S., Maurer, S.A., McLaughlin, P.F., Menger, M.F.S.J., Mewes, J.-M., Mewes, S.A., Morgante, P., Mullinax, J.W., Oosterbaan, K.J., Paran, G., Paul, A.C., Paul, S.K., Pavošević, F., Pei, Z., Prager, S., Proynov, E.I., Rák, Á., Ramos-Cordoba, E., Rana, B., Rask, A.E., Rettig, A., Richard, R.M., Rob, F., Rossomme, E., Scheele, T., Scheurer, M., Schneider, M., Sergueev, N., Sharada, S.M., Skomorowski, W., Small, D.W., Stein, C.J., Su, Y.-C., Sundstrom, E.J., Tao, Z., Thirman, J., Tornai, G.J., Tsuchimochi, T., Tubman, N.M., Veccham, S.P., Vydrov, O., Wenzel, J., Witte, J., Yamada, A., Yao, K., Yeganeh, S., Yost, S.R., Zech, A., Zhang, I.Y., Zhang, X., Zhang, Y., Zuev, D., Aspuru-Guzik, A., Bell, A.T., Besley, N.A., Bravaya, K.B., Brooks, B.R., Casanova, D., Chai, J.-D., Coriani, S., Cramer, C.J., Cserey, G., DePrince, A.E., III, DiStasio, R.A., Jr., Dreuw, A., Dunitz, B.D., Furlani, T.R., Goddard, W.A., III, Hammes-Schiffer, S., Head-Gordon, T., Hehre, W.J., Hsu, C.-P., Jagau, T.-C., Jung, Y., Klamt, A., Kong, J., Lambrecht, D.S., Liang, W., Mayhall, N.J., McCurdy, C.W., Neaton, J.B., Ochsenfeld, C., Parkhill, J.A., Peverati, R., Rassolov, V.A., Shao, Y., Slipchenko, L.V., Stauch, T., Steele, R.P., Subotnik, J.E., Thom, A.J.W., Tkatchenko, A., Truhlar, D.G., Van Voorhis, T., Wesolowski, T.A., Whaley, K.B., Woodcock, H.L., III, Zimmerman, P.M., Faraji, S., Gill, P.M.W., Head-Gordon, M., Herbert, J.M., Krylov, A.I., 2021. Software for the frontiers of quantum chemistry: An overview of developments in the Q-Chem 5 package. *The Journal of Chemical Physics* 155, 084801. <https://doi.org/10.1063/5.0055522>.

[42] Landau, A., Khistyayev, K., Dolgikh, S., n.d. Frozen natural orbitals for ionized states within equation-of-motion coupled-cluster formalism. *J. Chem. Phys.* 2010, 132, 014109.

[43] Neese F. Software update: The ORCA program system—Version 5.0. *WIREs Comput Mol Sci.* 2022; 12:e1606. <https://doi.org/10.1002/wcms.1606>.

[44] Cerezo, J., Santoro, F., FCClasses3, Vibrationally-resolved spectra simulated at the edge of the harmonic approximation, *J. Comput. Chem.* 2023, 44, 626.

[45] Lu, T., Chen, F., Multiwfn: A multifunctional wavefunction analyzer. *J. Comput. Chem.* 2012, 33, 580-592.

- [46] Drwal, D., Matousek, M., Golub, P., Tucholska, A., Hapka, M., Brabec, J., Veis, L., Pernal, K., 2023. Role of Spin Polarization and Dynamic Correlation in Singlet–Triplet Gap Inversion of Heptazine Derivatives. *J. Chem. Theory Comput.* 2023, 19, 7606-7616.
- [47] Schreiber, M., Silva-Junior, M.R., Sauer, S.P.A., Thiel, W., 2008. Benchmarks for electronically excited states: CASPT2, CC2, CCSD, and CC3. *The Journal of Chemical Physics* 128, 134110.
- [48] Sneskov, K., and Christiansen, O., Excited state coupled cluster methods, *WIREs Comput Mol Sci* 2011. doi: 10.1002/wcms.99.
- [49] Valverde, D., Cher Tian, S., Ricci, G., Jorner, K., Pollice, R., Aspuru-Guzik, A., and Olivier, Y., Computational Investigations of the Detailed Mechanism of Reverse Intersystem Crossing in Inverted Singlet–Triplet Gap Molecules, *ACS Appl. Mater. Interfaces* 2024, <https://doi.org/10.1021/acsami.4c04347>.
- [50] T. Northey and T.J. Penfold, *The intersystem crossing mechanism of an ultrapure blue organoboron emitter*, *Organic Electronics*, 2018, 59, 45-48.
- [51] T. J. Park, J. C. Light, *Unitary quantum time evolution by iterative Lanczos reduction*, *J. Chem. Phys.* 1986, 85, 5870–5876
- [52] A. Landi, R. Borrelli, A. Capobianco, A. Peluso, *Transient and Enduring Electronic Resonances Drive Coherent Long Distance Charge Transport in Molecular Wires*, *J. Phys. Chem. Lett.* 2019, 10, 1845–1851.
- [53] A. Landi, A. Landi, A. Leo, A. Peluso, *The rates of non-adiabatic processes in large molecular systems: Toward an effective full-dimensional quantum mechanical approach.*, *J. Chem. Phys.* 2024, 160, 174114.
- [54] R. Borrelli, A. Capobianco, A. Landi, A. Peluso, *Vibronic Couplings and Coherent Electron Transfer in Bridged Systems*, *Phys. Chem. Chem. Phys.* 2015, 17, 30937–30945.
- [55] A. Landi, G. Ricci, A. Capobianco, Y. Olivier and A. Peluso, *Towards Efficient TADF Modeling: Overcoming Computational Challenges in Quantum Dynamics Simulations*, *JPCL*, 2024, accepted